Tectonics

RESEARCH ARTICLE
10.1029/2019TC005585

Key Points:
- Illite polytype determinations allowed discriminating between authigenic/synkinematic and detrital illite crystals
- K-Ar ages of synkinematic illite indicate multiple reactivation for the Río Grío and Vallès-Penedès Faults during the Mesozoic and Paleogene
- Key stages of thermotectonic evolution of the Iberian Plate can be explained within the frame of K-Ar illite ages

Correspondence to:
L. Aldega,
luca.aldega@uniroma1.it

Citation:
Aldega, L., Viola, G., Casas-Sainz, A., Marcén, M., Román-Berdiel, T., & van der Lelij, R. (2019). Unraveling multiple thermotectonic events accommodated by crustal-scale faults in northern Iberia, Spain: Insights from K-Ar dating of clay gouges. *Tectonics*, *38*, 3629–3651. https://doi.org/10.1029/2019TC005585

Received 19 MAR 2019
Accepted 31 AUG 2019
Accepted article online 6 SEP 2019
Published online 16 OCT 2019

Unraveling Multiple Thermotectonic Events Accommodated by Crustal-Scale Faults in Northern Iberia, Spain: Insights From K-Ar Dating of Clay Gouges

L. Aldega[1], G. Viola[2], A. Casas-Sainz[3], M. Marcén[3], T. Román-Berdiel[3], and R. van der Lelij[4]

[1]Dipartimento di Scienze della Terra, Sapienza Università di Roma, Roma, Italy, [2]Dipartimento di Scienze Biologiche, Geologiche ed Ambientali – BiGeA, Università degli Studi di Bologna, Bologna, Italy, [3]Geotransfer (IUCA), Universidad de Zaragoza, Zaragoza, Spain, [4]Geological Survey of Norway, Trondheim, Norway

Abstract Large-scale faults in the continental crust are significant features that control the evolution of sedimentary basins and intraplate mountain chains. Deciphering their evolution is a significant task because faults slip and reactivate in a variety of geological settings. In this work, clay gouges of two major orogen-scale, long-lived faults in northern Iberia, the Río Grío and Vallès-Penedès Faults, were investigated by X-ray diffraction and K-Ar isotopic analysis. Illite polytype determinations of 44 subfractions (from <0.1 to 10 μm) allowed us to discriminate between authigenic/synkinematic illite crystals formed during faulting and detrital illite crystals inherited from the host rock. K-Ar dating provided a detailed set of ages corresponding to key stages of the thermotectonic evolution of the Iberian Plate: (a) the Permian to Late Triassic extensional/transtensional activity associated to the emplacement of Late Variscan magmatic bodies and hydrothermal mineralizations, (b) the opening of the Central Atlantic Rift during Late Triassic-Early Jurassic times, (c) the Late Jurassic-Early Cretaceous rifting that led to the development of Mesozoic extensional/transtensional basins in northern Iberia, (d) the final stage of the anticlockwise rotation of the Iberian Plate with respect to Eurasia and the accommodation of the first Pyrenean compressional pulses in Campanian time, and (e) the positive inversion of Mesozoic extensional basins due to far-field stresses associated with the Alpine orogeny during the Paleogene. The results highlight that thermotectonic conditions characterized by high-geothermal gradients strongly favor fault movement and neoformation of clay minerals in fault gouges, regardless of the prevailing tectonic regime.

1. Introduction

Fault zones are natural archives of crustal tectonic histories and of the prevailing physical and chemical conditions at the time of brittle deformation (Viola et al., 2016). This is because, once formed, faults may be extremely sensitive to variations of the stress field and environmental conditions and are prone to slip and reactivate in a variety of geological settings even in regions affected by weak far-field stresses. In addition, multiple reactivated faults do not necessarily conform to theoretical length-displacement relationships (Schultz et al., 2006). Multiple reactivations and long slip histories may lead to extremely complex fault architectures, the unraveling of which remains challenging in the absence of solid time constraints. Hence, the study of fault zones by K-Ar isotopic dating of authigenic/synkinematic illite coupled with X-ray diffraction of clay gouges may offer a unique possibility to decipher protracted brittle deformation, the details of which could otherwise remain hidden in the rock record.

One major tectonic system formed by long-lived orogen-scale faults is the so-called "Late Variscan fracturing system" of the Iberian Plate, inherited from the Carboniferous Variscan orogeny. The Late Variscan structural configuration conditioned the architecture of Mesozoic and Cenozoic basins and evolution of the plate during both periods (Arthaud & Matte, 1977; Alvaro et al., 1979; Ziegler, 1982; Kronberg, 1991; Gomes et al., 2007; Figure 1a). This makes the Iberian Plate an interesting area where to test techniques aimed at studying crustal-to-lithospheric-scale faults.

The details of the complex kinematic history of many large faults of the Iberian Plate during the Mesozoic remain still poorly understood because, once formed, faults have been overprinted by either Mesozoic

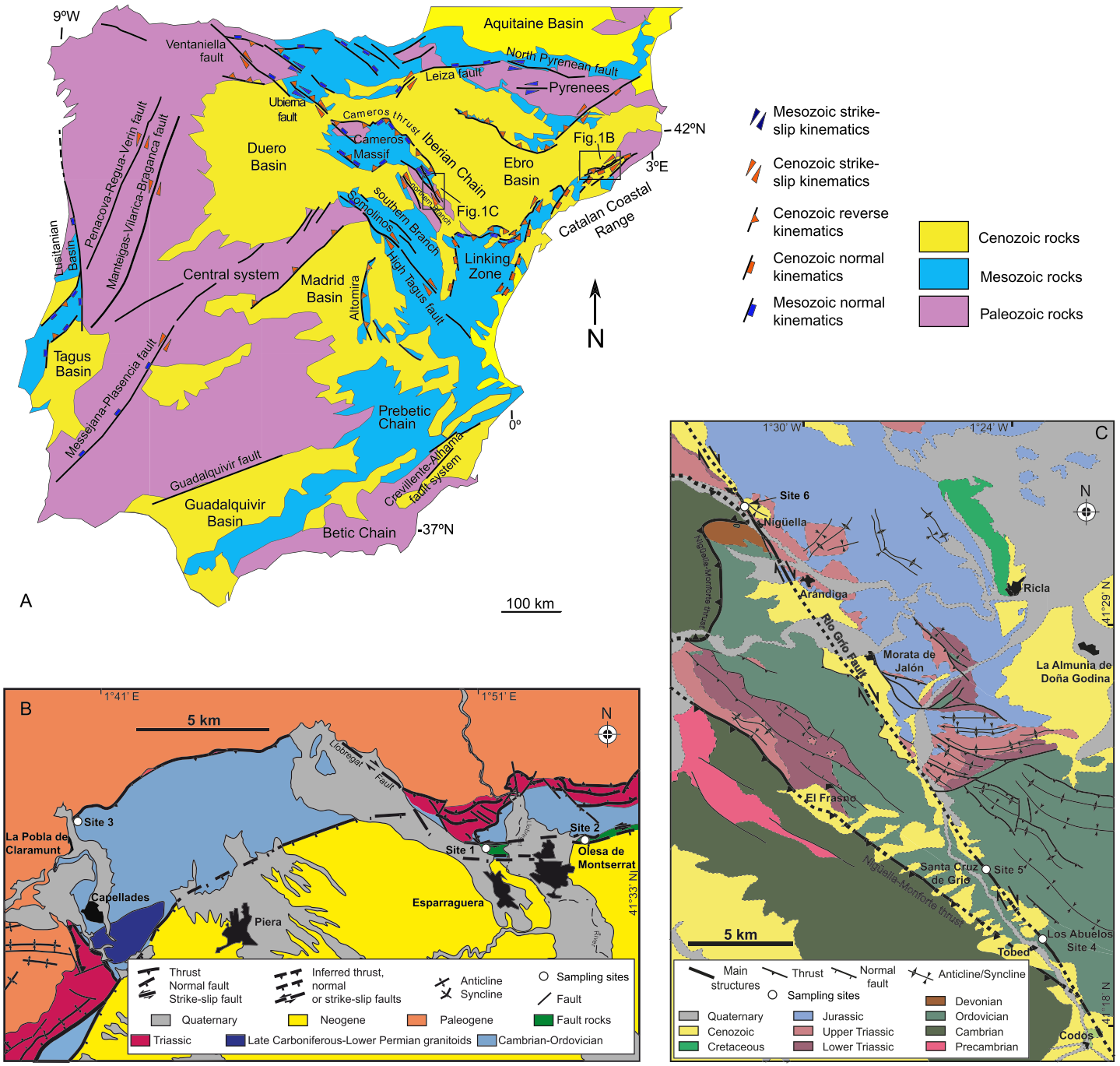

Figure 1. (a) Crustal- and lithospheric-scale faults in the Iberian Peninsula (most of them having a Late Variscan origin). Boxes indicate the studied faults. (b) Geological sketch map of the central segment of the Vallès-Penedès Fault with sampling sites (after Marcén et al., 2018, modified). (c) Geological sketch map of the Río Grío Fault with sampling sites.

extensional tectonics or positive inversion during the Cenozoic (Eocene to Miocene, depending on their location within the Iberian Plate, e.g., Casas Sainz, 1993; Cortés et al., 1999; Salas et al., 2001; De Vicente et al., 2009). Further complexity was added by the negative inversion during the Oligocene and Miocene linked to the evolution of the eastern margin of Iberia and the opening of the València Trough (Fontboté et al., 1990; Vegas, 1992).

Faults of the "Late Variscan fracturing system," characterized by a dominant strike-slip component, formed by switching of the σ_2 and σ_3 principal stress axes with variable contributions of escape tectonics after the

main stage of crustal thickening (Picha, 2002; Tapponnier et al., 1986; Tapponnier & Molnar, 1976). Locally, normal faults formed as a result of extensional collapse (and switching between σ_2 and σ_1 stress axes) of some sectors of the Variscan orogen (see, e.g., Malavieille, 1993; Doblas et al., 1994; Román-Berdiel et al., 1995; Llana-Fúnez & Marcos, 2001; Marques et al., 2002). Traditionally, the Permian (and also the Late Carboniferous, e.g., Cantarelli et al., 2013) is considered the main stage of Variscan post-orogenic extensional faulting, also associated with volcanism of mantle origin (Lago et al., 2004a, 2004b). However, hydrothermal mineralizations connected to this event in the Iberian Plate point to a more complex and longer evolution suggesting multiple deformation stages. These stages are related to the opening of the Central Atlantic during Middle to Late Triassic (Pocoví et al., 1990) or even Middle Jurassic times (Palencia-Ortas et al., 2006, and references therein).

The details of the transition from an extensional to a compressional regime in the Iberian Plate during the Late Mesozoic and Cenozoic are still poorly constrained. No known sedimentary record directly attests to the transition from rift tectonics (believed to be dominant from the Permian to the Triassic, Jurassic, and Early Cretaceous) to clear compressional tectonics (starting during the Late Cretaceous, e.g., Martinez-Peña & Casas-Sainz, 2003, and references therein). The Early to Late Cretaceous corresponds to plate reorganization and volcanism at the global scale (Matthews et al., 2012; Scotese et al., 1988; Seton et al., 2012). Both phenomena are matched by important, regional-scale events in the western Tethys, such as the well-constrained remagnetization event of the basins of the High Atlas (African Plate, e.g., Torres-López et al., 2014; Moussaid et al., 2015) and of the Iberian Chain (Iberian Plate, e.g., Juárez et al., 1994, 1996, 1998; Villalaín et al., 2003; Soto, Villalaín, & Casas-Sainz, 2008).

Additionally, the timing of some of the post-Permian events affecting the Iberian Plate is also controversial because of the discrepancies between the chronological constraints provided by ocean floor magnetic anomalies (Rosenbaum et al., 2002) on the one hand and by paleomagnetic data (Gong et al., 2008; Neres et al., 2012) on the other. While paleomagnetic data point to a counterclockwise rotation of the plate during Aptian times (e.g., Gong et al., 2009), models based on magnetic anomalies of the ocean floor (Srivastava et al., 2000) indicate instead a more gradual and longer process (see Seton et al., 2012, and references therein).

Available fission-track data on zircon and apatite and U-Th/He ages on apatite for the Iberian Plate record the last period of cooling during the Alpine compression. Moreover, they suggest slow cooling throughout the Jurassic and thermal stability during the Late Cretaceous for the Iberian Chain and Catalan Coastal Range (De Bruijne & Andriessen, 2002; Del Río et al., 2009; Juez-Larré & Andriessen, 2006).

In this work we aim at providing absolute time constraints for the thermotectonic events responsible for the structuring and evolution of the Iberian Plate in post-Variscan times, especially during the Mesozoic. For this purpose, we have dated fault gouges from two crustal-scale fault zones of the northern Iberian Plate: the Río Grío Fault in the Iberian Chain and the Vallès-Penedès Fault in the Catalan Coastal Range (Figure 1). The new K-Ar dates derived from authigenic and synkinematic illite separated from structurally well-constrained gouge samples allow us to propose an evolutionary model of these important faults, wherein we can identify and constrain in time a series of slip events that would otherwise remain hidden in the faults' structural record.

These faults are long-lived deformation zones active since the Paleozoic. Their polyphase tectonic activity played a major role in the location, development, and control of the architecture of Mesozoic and Cenozoic sedimentary basins. Our results are crucial to the further development of existing tectonic reconstructions based upon their detailed study, involving structural, magnetic, and multiscalar structural analysis (Marcén et al., 2018).

2. Geological Setting: The Vallès-Penedès and Río Grío Faults

The Vallès-Penedès and Río Grío Faults are excellent examples of crustal-scale faults that steered the geometric and kinematic evolution of the Catalan Coastal and Iberian Ranges, respectively (Figures 1b and 1c). These two mountain chains, together with the Central System (De Vicente et al., 2007; De Vicente & Muñoz-Martín, 2013), are the areas where deformation localized in the inner part of the Iberian Plate in response to far-field stresses transferred from the plate margins.

The Catalan Coastal Range is a thick-skinned belt that strikes predominantly NE-SW and is controlled by large-scale thrusts such as the Vallès-Penedès Fault (Marcén et al., 2018, and references therein). Cenozoic extensional tectonics responsible for the opening of the València Trough reactivated the NE-SW striking fault system as normal faults, both in the Catalan Coastal Range and in the Eastern Iberian Range (Antolín-Tomás et al., 2007; Roca et al., 1999).

The Vallès-Penedès Fault has an outcropping length of more than 100 km onshore, and it propagates in the marine platform of the València Trough with the same NE-SW direction. It hosts a prominent gouge fault core up to 500 m thick (Santanach & Julià, 1984). As in the Iberian Chain, subsequent negative and positive inversions of the precursor Late Variscan, crustal-scale discontinuities controlled the evolution of the Catalan Coastal Range during the Mesozoic and Cenozoic. Although deformational or synsedimentary records of this Late Variscan period are not preserved, the emplacement of fault-parallel, early-Triassic magmatic bodies of subcrustal origin (Institut Cartogràfic de Catalunya, 2006a, 2006b) and mineralizations along the range (Canals & Ayora, 1988; Canals & Cardellach, 1997) were probably favored by these crustal discontinuities. The distribution of Triassic depocenters (Sopeña et al., 1983) along the Vallès-Penedès Fault and the different thickness of the Mesozoic series in each fault block (Institut Cartogràfic de Catalunya, 2005; Marín et al., 2008; Roca, 1994) indicate that subsidence during Mesozoic time was controlled by the activity of this fault. The subsequent Paleogene N-NNW/S-SSE shortening produced positive inversion of the Mesozoic structures and uplift of the Catalan Coastal Range (Anadón et al., 1979; Fontboté, 1954; Llopis Lladó, 1947; Roca et al., 1999). The Vallès-Penedés Fault contains kinematic indicators (e.g., asymmetric foliation, slickensides, SC structures, and anisotropy of magnetic susceptibility data; see Marcén et al., 2018) indicative of sinistral and reverse slips under a transpressive regime during the Paleogene. Finally, negative tectonic inversion during the Oligocene-Miocene affected the easternmost part of the fault zone, which was reactivated in an extensional fashion, leading to discrete normal faults. These more localized faults cut through the earlier fault cores, defined by fault gouge, and the damage zones (Marcén et al., 2018). In addition to the main fault plane bounding the Neogene extensional basin, which accommodated a dip-slip normal displacement of several thousands of meters, minor discrete fault planes also occur. These can be several meters long and accommodate centimetric displacements as evidenced by deflected structural markers.

The Iberian Chain strikes predominantly NW-SE (Figures 1a and 1c) and is characterized by widespread occurrences of Paleozoic rocks, bounded by steeply dipping faults (Cortés-Gracia & Casas Sainz, 1996; De Vicente et al., 2009). The most prominent thrust systems of the chain reflect a thin-skinned style, with the major thrusts detaching on low-strength Upper Triassic shales and evaporites. Thrusts generally trend NW-SE but become E-W, at both the northwestern and southeastern terminations of the chain (Casas-Sainz et al., 2017; Guimerà, 1984). They are N-S in the Altomira Range. A thick-skinned structural style, with basement-involving thrusts accommodating horizontal displacements of up to 25 km and vertical displacements of up to 4 km (Casas Sainz, 1993), also dominates in several segments of the Iberian Chain (De Vicente, 2018; Liesa et al., 2018).

The Río Grío Fault is the northernmost outcropping large-scale fault of the Iberian Chain and defines the shape of its northern (Aragonian) Branch (Figure 1a). It crops out for more than 100 km along strike with a general NNW-SSE trend bordering the most important intracontinental rift basin in Western Europe (Cameros Basin). Its trace partly coincides with one of the most important Variscan thrusts of the Iberian Chain, the Nigüella-Monforte Thrust (Calvín-Ballester & Casas, 2014), which accommodated kilometer-scale, top-to-the-NE displacement. The Late and post-Variscan evolution of the Río Grío Fault is documented by mineralizations that are hosted along its trace within Paleozoic and Triassic rocks (Pocoví et al., 1990) as well as Permian volcanites (Lago et al., 2004a). Moreover, tectonic slivers formed by Triassic rocks that can be interpreted as strike-slip duplexes are found in the fault zone. Cataclasite and gouge are found in a heterogeneous, up to 200 m thick deformation zone that also contains large blocks of relatively less-deformed pre-Variscan, Permian, and Triassic rocks containing a subvertical foliation bearing both horizontal and dip-slip lineation. Its complex deformation history includes dextral and reverse slips associated with late transpressive movement during Cenozoic compression (Marcén & Román Berdiel, 2015). Quaternary reactivation has been also documented (Casas-Sainz et al., 2018, and references therein) and controls the morphology of the area, characterized by longitudinal valleys parallel to the fault.

3. Methods

The analytical procedures for separating, characterizing, and dating the samples are described in detail in Viola et al. (2018) and represent the current routine workflow at the recently established laboratory for clay characterization and K-Ar dating at the Geological Survey of Norway, Trondheim. Particle sizes of <0.1, 0.1–0.4, 0.4–2, 2–6, and 6–10 μm were generated using sedimentation with Stokes law and a combination of continuous flow and fixed angle rotor centrifuges. Ar was extracted from clay aliquots packed in Mo foil in a stainless steel ultrahigh vacuum line using a Pond Engineering furnace at 1400 °C. The evolved sample gas was purified in a first stage using a titanium sublimation pump, and in a second stage with one SAES GP50 getter at room temperature and one SAES GP50 getter at 350 °C. Sample gas was spiked with approximately $2*10^{-13}$ moles of pure ^{38}Ar (Schumacher, 1975) and analyzed in an IsotopX NGX multicollector noble gas mass spectrometer fitted with five faraday cups for 600 integrations of 1 s each. Nominal argon beam intensities were determined by using a degree 2 polynomial regression to the time the sample was let into the mass spectrometer, with an in-house Python program. Beam intensities for ^{38}Ar and ^{36}Ar were corrected for mass discrimination relative to ^{40}Ar by a power law (e.g., Renne et al., 2009), using the weighted mean $^{40}Ar/^{36}Ar$ ratios of 299.781 ± 0.014 measured from atmospheric argon in an online air pipette. Radiogenic $^{40}Ar^*$ concentrations and their uncertainties were calculated using the equations outlined in Hałas and Wójtowicz (2014) using the atmospheric argon composition of Lee et al. (2006). Within this analytical batch, four aliquots of GA-1550 biotite (98.5 ± 0.5 Ma; McDougall & Wellman, 2011) were analyzed and yielded a weighted mean age of 98.53 ± 0.36 Ma. Potassium concentrations were determined by fusing an aliquot of approximately 50 mg in lithium tetraborate at ~1000 °C to form a glass, which was then dissolved in HNO_3 with a rhodium internal standard at 5 ppm prior to analysis with a Perkin Elmer Optima 4300 DV ICP-OES. K-Ar dates were calculated using the ^{40}K abundance and decay constants of Steiger and Jäger (1977).

X-ray diffraction analyses were performed on a Scintag X1 X-ray system (CuKα radiation) at 40 kV and 45 mA. Randomly oriented whole-rock powders were run in the 2–70° 2θ interval with a step size of 0.05° 2θ and a counting time of 3 s per step. Oriented air-dried and ethylene-glycol solvated samples of the <2 μm grain size fraction were scanned from 1° to 48° 2θ and from 1° to 30° 2θ respectively with a step size of 0.05° 2θ and a count time of 4 s per step. The presence of expandable clays was determined for samples treated with ethylene-glycol at 25 °C for 24 hr. The illite content in mixed layers illite-smectite (I-S) was determined according to Moore and Reynolds (1997) using the delta two-theta method after decomposing the composite peaks between 9–10° 2θ and 16–17° 2θ. The I-S ordering type (Reichweite parameter, R; Jagodzinski, 1949) was determined by the position of the I001-S001 reflection between 5° and 8.5° 2θ (Moore & Reynolds, 1997). Integrated peak areas of clay minerals and polytype $2M_1$ and $1M_d$ reflections were transformed into mineral concentration by using mineral intensity factors as a calibration constant (for a review, see Moore & Reynolds, 1997). Standard patterns for illite $1M_d$, 1M, and $2M_1$ polytypes were represented by the pure illites PDU, RM30, and SG4 (Eberl et al., 1987), respectively.

4. Results

4.1. Fault Zone Architectures and Sample Description

The sampled areas correspond to the core of the two studied faults. In each of them, samples were taken at three different sites sampling representative structural domains/fault facies. In the following we characterize each of the two faults, providing a detailed description of their architecture where sampled.

4.1.1. Vallès-Penedès Fault

The Vallès-Penedès Fault is a NE-SW striking basement fault dipping to the SE and accommodating a normal displacement of up to 4 km during the Neogene extension (Roca et al., 1999). The fault zone exhibits a banded heterogenous and anastomosing internal structure with pervasive slaty cleavage that coarsely mimics the strike of the fault trace, changing from WNW-ESE in the westernmost part of the Els Blaus outcrop (Site 1; Figure 1b) to ENE-WSW in the Ribes Blaves outcrop (Site 2) and to NE-SW in the La Pobla de Claramunt sector (Site 3).

The three sampled sites along the Vallès-Penedès Fault are representative of different structural settings within the core of the fault zone (Figure 1b). Site 1 (Els Blaus) is located at the intersection zone between a NW-SE lineament (perpendicular to the main trend of the mountain range) and the NE-SW trending

Vallès-Penedès Fault. This area coincides with the maximum width of the fault zone (several hundreds of meters), which mostly consists of blocks of Cambrian-Ordovician rocks and to a lesser extent of Triassic rocks, embedded within a scaly fault gouge of grayish color, mostly derived from the Paleozoic host rocks (LA73 and FV11, Figure 2a). Foliation planes are generally E-W and dip subvertically, oblique to the trace of the main fault. Quartz rods and fragments with striated surfaces derived from the host rock are frequently observed within the fault gouge. Slickensides and SC structures indicate complex reverse and strike-slip kinematics consistent with an overall transpressional regime for the fault zone. Strong partitioning of a reverse and strike-slip component on different surfaces within the fault zone is suggested by the study of magnetic fabrics (Marcén et al., 2018). Negative tectonic inversion during the Oligocene-Miocene extension affected the easternmost part of the fault zone. At Site 2 (Ribes Blaves), several hundred meters of fault gouge are found with strong similarities to Site 1. A subvertical, E-W foliation is present, oblique to the trace of the main fault, and kinematic indicators constrain sinistral displacement (LA74, Figure 2b). Finally, at the westernmost site (Site 3; La Pobla de Claramunt) the gouge of the fault core (sample LA76) indicates reactivation during thrusting along a fault surface with a WNW-ESE strike that juxtaposes Triassic and Paleozoic rocks in the hanging wall against Paleogene rocks in the footwall. The fault zone is here much thinner than at the other sampled sites (less than 50 m), probably because it is cut by the more recent thrusting. A subhorizontal foliation, parallel to the thrust plane, is dominant in the fault rocks (Figure 2c). More detailed outcrop descriptions can be found in Marcén et al. (2018).

4.1.2. Río Grío Fault

In the case of the Río Grío Fault, the sampled fault core at the Los Abuelos site (Site 4, Figure 2d; Figure 1c for location) is characterized by a NE-dipping, NW-SE striking, gently anastomosed fault array where displacement and deformation are distributed and partitioned into several fault strands. The core of each of these fault strands is defined by black and red clay-rich gouges formed at the expenses of Ordovician (LA77 and RG90) and Triassic (LA78) host rocks, respectively, and frequently mixed in the same fault gouge sample (Figure 2e). These fault cores are flanked by brecciated volumes containing metric to decametric blocks of quartzite. Fault rocks are generally foliated, with foliation planes dipping vertically to subvertically. Moderately plunging folds in the slivers of Paleozoic and Triassic rocks entrained along the fault are likely the expression of the transpressional deformation accommodated by the fault during the Cenozoic. The Santa Cruz de Grío site (Site 5) also displays an anastomosed fault zone architecture similar to that of the Los Abuelos site. Kinematic indicators (mainly SC structures and vertical asymmetrically arranged foliations) are compatible with a dextral strike-slip movement of the fault. The fault core sampled there is derived from Ordovician black shales and Triassic red beds, and well documents by means of SC fabrics the overall dextral kinematics (LA82, Figure 2f). Finally, the fault core at the northernmost site (Nigüella, Site 6) displays a subvertical south-dipping foliation developed in red and white gouge derived from Triassic host rocks (LA83, Figure 2g). In this case, the fault rocks are unconformably overlain by horizontal, Pliocene to Quaternary piedmont deposits. The thin, clayey core of the fault is surrounded by a fine-grained breccia that separates the Triassic dolostones in the southern block of the fault from Triassic red beds in its northern block.

4.2. X-ray Diffraction Analysis

The results of X-ray semiquantitative analysis of the clay gouges for the Vallès-Penedès and Río Grío Faults are shown in Figures 3 and 4 and Tables 1 and 2.

4.2.1. Vallès-Penedès Fault

Subfractions from the Vallès-Penedès Fault are derived from gouges (LA73, LA74, LA76, and FV11) formed at the expense of Ordovician rocks. The whole-rock composition of the former gouges is characterized by chlorite as the major constituent of the coarse fractions (2–6 and 6–10 μm) with contents ranging from 27% to 66% (Figure 3, Table 1). K-bearing minerals in these grain size fractions are illite/muscovite-$2M_1$ with contents between 15% and 33% and K-feldspar not exceeding 4%. Na-plagioclase and kaolinite <3% occur in the coarse fractions whereas calcite is only sporadically found in sample LA76. Large variations of quartz content in the studied samples (from 1% to 53%) are related to the strong fragmentation of the highly heterogeneous quartz rods and fragments that are present in the rock fault matrix (Figure 2a).

The general and progressive decrease of chlorite, quartz, and illite/muscovite-$2M_1$ contents in the finer grain size fractions (<0.1, 0.1–0.4, and 0.4–2 μm; see Figure 3) is compensated by the neoformation of illite-$1M_d$

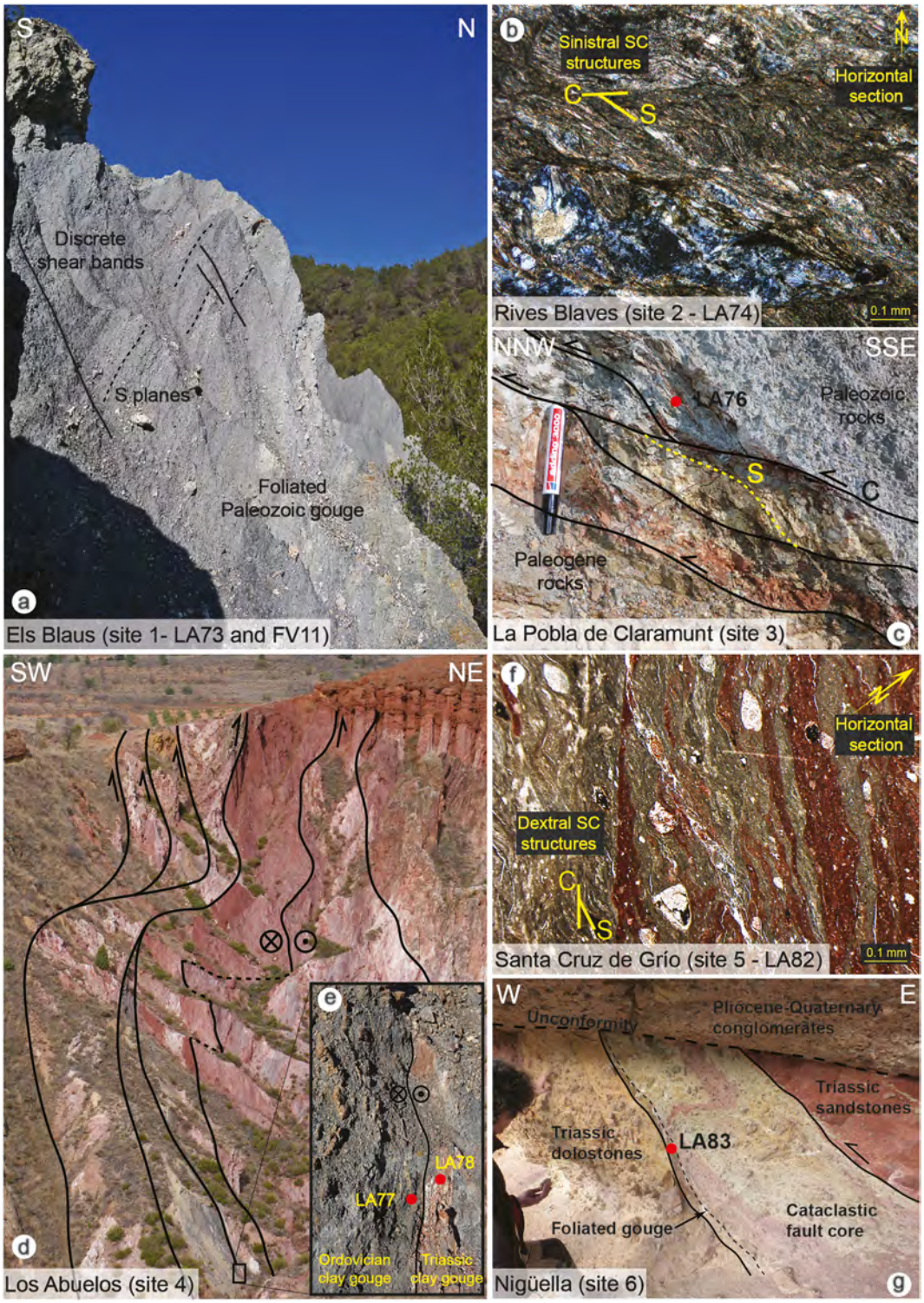

Figure 2. Outcrop photos of the Vallès-Penedès (a–c) and Río Grío (d–g) Faults. (a) Vallès-Penedès Fault (Els Blaus, Site 1; see Figure 1b for location) with a thick-foliated gouge containing centimeter- to meter-scale quartz rods and fragments. (b) Thin section of the Paleozoic rocks in the Rives Blaves outcrop (Site 2) showing sinistral SC structures. (c) Vallès-Penedès Fault in the La Pobla de Claramunt (Site 3) showing the juxtaposition of Paleozoic rocks above Paleogene rocks. (d) Architecture of the Río Grío Fault at Los Abuelos (Site 4), close to Tobed village (see Figure 1c for location). (e) Close-up of the Río Grío fault core with sampling location. (f) Thin section microphotograph of the Río Grío Fault core at Santa Cruz de Grío (Site 5) showing dextral SC structures. (g) Fault architecture at Nigüella (Site 6; see Figure 1c for location) showing red and white gouges derived from Triassic host rocks unconformably overlain by Pliocene to Quaternary conglomerates.

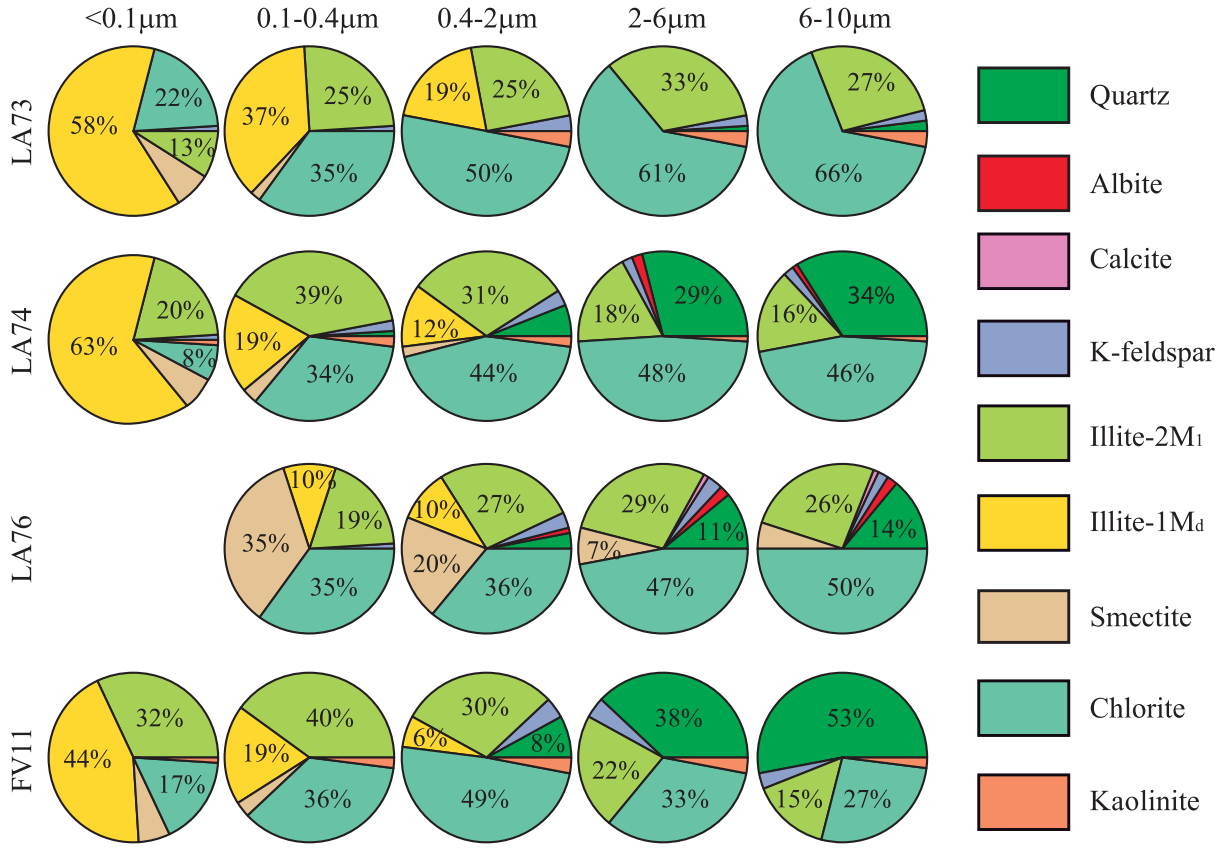

Figure 3. X-ray semiquantitative analysis of clay gouges for the Vallès-Penedès Fault. Samples LA73 and FV11 are from the Els Blaus outcrop (Site 1); LA74 is from the Rives Blaves outcrop (Site 2), and LA76 from the La Pobla de Claramunt sector (Site 3; see Figure 1b for location).

and smectite. Illite-1M_d and smectite are the dominant clay minerals in the <0.1 μm fractions forming at least 50% of the whole-rock mineralogical assemblage (Figure 3, Table 1).

4.2.2. Río Grío Fault

X-ray diffraction analyses for gouges derived from brittle deformation of Triassic (LA78 and LA83) and Ordovician (LA77, LA82, and RG90) rocks from the Río Grío Fault are shown in Figure 4 and Table 2. The mineralogical assemblage of LA78 and LA83 gouges in the 2–6 and 6–10 μm grain size fractions is mainly defined by quartz, illite/muscovite-2M_1, and kaolinite, whose contents vary between 85% and 95% of the overall composition. Low K-feldspar (<3%), hematite (<3%), and chlorite (<6%) contents have also been documented in the coarse fractions. Mixed layers I-S occur only in sample LA83 with contents lower than 3%.

Quartz and kaolinite become progressively less abundant in the finer fractions (<0.1, 0.1–0.4, and 0.4–2 μm) where a general increase of illite-1M_d and long range ordered (R3) mixed layers I-S is instead observed from 7% to 62% and from 7% to 26%, respectively. Illite-1M_d and illite/muscovite-2M_1 are the dominant clay minerals in the <0.1 μm fraction constituting at least 69% of the whole-rock mineralogical assemblage. No other K-bearing minerals were observed in this fraction.

Undeformed rocks were collected 0.8–3 km far away from the fault in the Lower Triassic pelitic red beds of the Iberian Basin to compare and contrast the levels of thermal maturity due to sedimentary burial and faulting. X-ray diffraction patterns for randomly oriented whole-rock powders display a mineralogical assemblage characterized by phyllosilicate minerals with contents between 71% and 78% and subordinate amounts of quartz (10–18%), hematite (9%), and dolomite (<6%; Table 3). Traces of gypsum have been locally observed. In the oriented patterns of the <2 μm grain size fraction, illite is the major clay mineral with contents between 76% and 91% followed by mixed layers I-S (6–20%) and kaolinite (3–6%). Mixed layers I-S are long range ordered structures (R3) with an illite content of 87% indicating thermal maturity consistent with

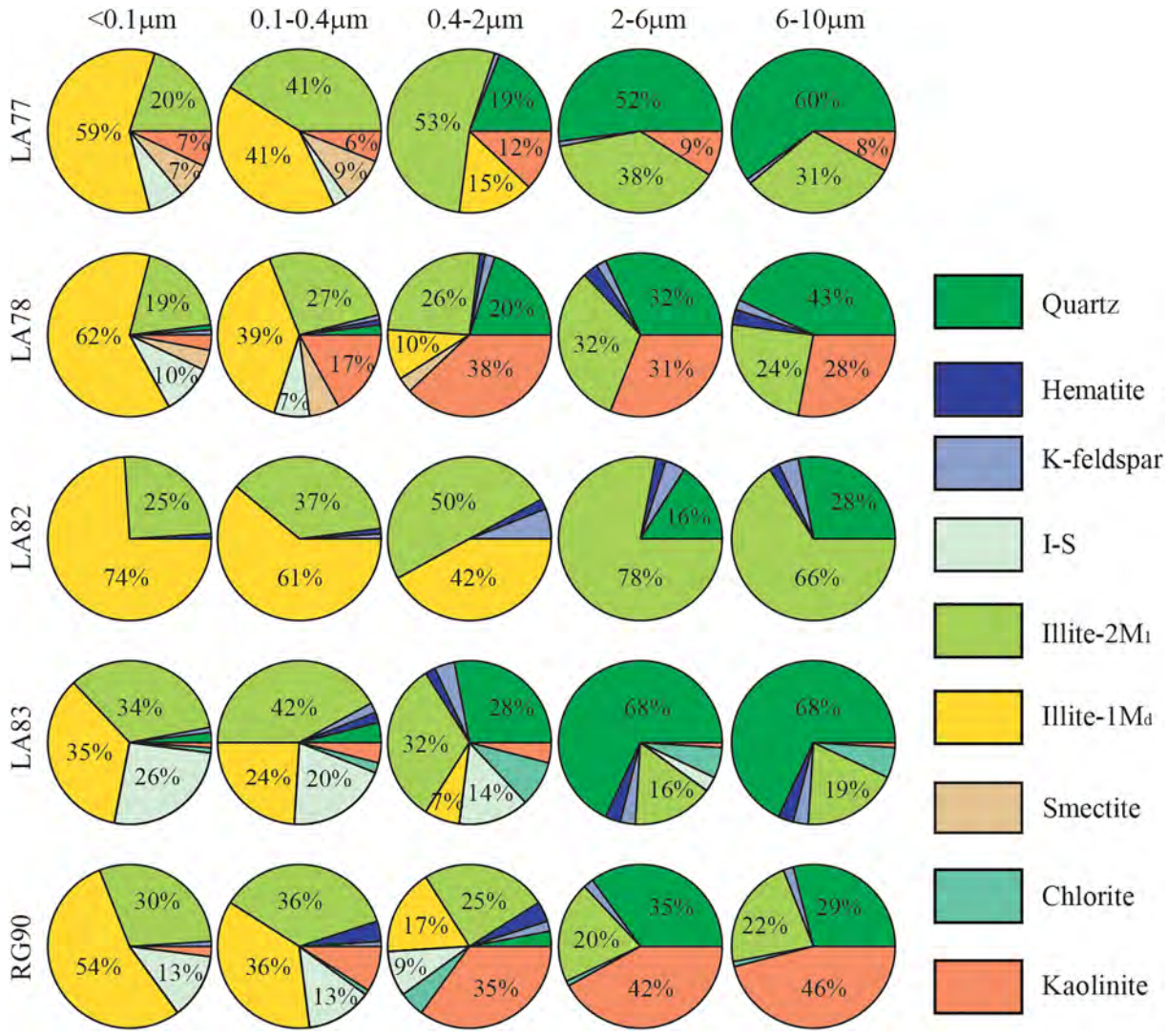

Figure 4. X-ray semiquantitative analysis of clay gouges for the Río Grío Fault. Samples LA77, LA78, and RG90 are from the Los Abuelos outcrops (Site 4), LA82 is from Santa Cruz de Grío (Site 5), and LA83 from the Nigüella outcrops (Site 6; see Figure 1c for site location).

late diagenetic conditions and shallow burial depths (Aldega et al., 2007). The occurrence of low expandable mixed layers I-S with similar stacking order and illite layers in the fault rocks subfractions suggests that brittle deformation occurred at depths (and temperature) similar to those recorded by the undeformed rocks.

LA77, LA82, and RG90 gouges formed by brittle deformation at the expense of Ordovician rocks are mainly characterized by quartz and illite/muscovite-2M_1 with contents >90% in the coarse subfractions, by variable amounts of kaolinite (up to 46%) and by subordinate contents of K-feldspar (<6%) and hematite (2%). In the finer fractions, illite-1M_d and illite/muscovite-2M_1 are the dominant clay minerals followed by low amounts of mixed layers I-S, smectite, and kaolinite (Figure 4).

4.3. K-Ar Geochronology

4.3.1. Vallès-Penedès Fault

Five clay size fractions were analyzed with K-Ar geochronology for each of the four samples dated in this study (Table 4 and Figure 5a). Almost invariably there is a direct grain size-age correlation, wherein the coarser the dated grain size fraction, the older the age (Figure 5a). For sample LA73, the <0.1 μm fraction yields a date of 104.5 ± 1.3 Ma, the 0.1–0.4 μm fraction a date of 164.4 ± 2.0 Ma, the 0.4–2 μm fraction a date of 216.3

Table 1
Whole-Rock Composition of Various Grain Size Fractions for Gouges of the Vallès-Penedès Fault

	Whole-rock composition (wt%)								
Sample ID	Qtz	Ab	Kfs	Cal	I-2M$_1$	I-1M$_d$	Sm	Chl	Kln
LA73_6-10	2	—	2	—	27	—	—	66	3
LA73_2-6	1	—	2	—	33	—	—	61	3
LA73_0.4-2	—	—	3	—	25	19	—	50	3
LA73_0.1-0.4	—	—	1	—	25	37	2	35	—
LA73_<0.1	—	—	1	—	13	58	6	22	—
LA74_6-10	34	1	2	—	16	—	—	46	1
LA74_2-6	29	2	2	—	18	—	—	48	1
LA74_0.4-2	6	—	3	—	31	12	2	44	2
LA74_0.1-0.4	1	—	2	—	39	19	3	34	2
LA74_<0.1	—	—	1	—	20	63	7	8	1
LA76_6-10	14	2	2	1	26	—	5	50	—
LA76_2-6	11	2	3	1	29	—	7	47	—
LA76_0.4-2	3	1	3	—	27	10	20	36	—
LA76_0.1-0.4	—	—	1	—	19	10	35	35	—
FV11_6-10	53	—	3	—	15	—	—	27	2
FV11_2-6	38	—	4	—	22	—	—	33	3
FV11_0.4-2	8	—	4	—	30	6	—	49	3
FV11_0.1-0.4	—	—	—	—	40	19	3	36	2
FV11_<0.1	—	—	—	—	32	44	6	17	1

Note. Ab = albite; Cal = calcite; Chl = chlorite; I-1M$_d$ = illite-1M$_d$; I-2M$_1$ = illite-2M$_1$; Kfs = K-feldspar; Kln = kaolinite; Qtz = quartz; Sm = smectite.

Table 2
Whole-Rock Composition of Various Grain Size Fractions for Gouges of the Río Grío Fault

	Whole-rock composition (wt%)								
Sample ID	Qtz	Kfs	Hem	I-2M$_1$	I-1M$_d$	I-S	Sm	Chl	Kln
LA77_6-10	60	1	—	31	—	—	—	—	8
LA77_2-6	52	1	—	38	—	—	—	—	9
LA77_0.4-2	19	1	—	53	15	—	—	—	12
LA77_0.1-0.4	—	—	—	41	41	3	9	—	6
LA77_<0.1	—	—	—	20	59	7	7	—	7
LA78_6-10	43	2	3	24	—	—	—	—	28
LA78_2-6	32	2	3	32	—	—	—	—	31
LA78_0.4-2	20	2	1	26	10	—	3	—	38
LA78_0.1-0.4	2	1	1	27	39	7	6	—	17
LA78_<0.1	1	1	—	19	62	10	4	—	3
LA82_6-10	28	4	2	66	—	—	—	—	—
LA82_2-6	16	4	2	78	—	—	—	—	—
LA82_0.4-2	—	6	2	50	42	—	—	—	—
LA82_0.1-0.4	—	1	1	37	61	—	—	—	—
LA82_<0.1	—	—	1	25	74	—	—	—	—
LA83_6-10	68	3	3	19	—	tr	—	6	1
LA83_2-6	68	3	3	16	—	3	—	6	1
LA83_0.4-2	28	4	2	32	7	14	—	9	4
LA83_0.1-0.4	4	2	2	42	24	20	—	2	4
LA83_<0.1	2	1	—	34	35	26	—	1	1
RG90_6-10	29	2	tr	22	—	—	—	1	46
RG90_2-6	35	2	tr	20	—	—	—	1	42
RG90_0.4-2	3	2	4	25	17	9	—	5	35
RG90_0.1-0.4	—	1	4	36	36	13	—	1	9
RG90_<0.1	—	1	—	30	54	13	—	—	2

Note. Chl = chlorite; Hem = hematite; I-1M$_d$ = illite-1M$_d$; I-2M$_1$ = illite-2M$_1$; I-S = mixed layers illite-smectite; Kfs = K-feldspar; Kln = kaolinite; tr = traces (<1%); Qtz = quartz; Sm = smectite.

Table 3
Whole-Rock Composition and X-ray Diffraction Analysis of the <2 μm Grain Size Fraction for the Undeformed Triassic Rocks Exposed in the Iberian Basin

Sample ID	Age	Whole-rock composition (wt%)						<2 μm grain size fraction (wt%)					
		Qtz	Cal	Dol	Phy	Gy	Hem	I	I-S	C-S	Kln	R	%I in I-S
GT1	Triassic	18	—	—	73	tr	9	91	6	—	3	3	87
GT3	Triassic	14	—	6	71	tr	9	86	8	—	6	3	87
GT4	Triassic	10	—	3	78	—	9	76	20	—	4	3	87
GT5	Triassic	1	1	1	87	1	9	47	3	41	9	3	87

Note. %I in I-S = illite content in mixed layers illite-smectite; Cal = calcite; C-S = mixed layers chlorite-smectite; Dol = dolomite; Gy = gypsum; Hem = hematite; I = illite; I-S = mixed layers illite-smectite; Phy = phyllosilicates; Qtz = quartz; R = I-S stacking order; tr = stands for traces (<1%).

± 2.6 Ma, the 2–6 μm fraction a date of 274.5 ± 2.6 Ma, and, finally, the 6–10 μm split a date of 283.8 ± 3.7 Ma. Sample LA74 yielded K-Ar dates of 195.5 ± 2.7 Ma, 250.5 ± 3.1 Ma, 292.5 ± 3.7 Ma, 318.5 ± 4.5 Ma, and 314.3 ± 4.7 Ma for the <0.1, 0.1–0.4, 0.4–2, 2–6, and 6–10 μm splits, respectively. Sample LA76 yielded identical dates to LA74 within error, with 197.9 ± 4.1 Ma, 254.1 ± 3.4 Ma, 295.5 ± 3.8 Ma, 317.2 ± 4.2 Ma, and 318.1 ± 4.4 Ma for the <0.1, 0.1–0.4, 0.4–2, 2–6, and 6–10 μm fractions, respectively.

Sample FV11 has a statistically identical K-Ar date for the finest <0.1 μm fraction to LA73 (102.2 ± 4.1 Ma), whereas for all other fractions it yielded remarkably younger dates than the other three samples (145.4 ± 1.9 Ma, 178.6 ± 2.3 Ma, 177.5 ± 2.6 Ma, and 191.5 ± 2.9 Ma, for the 0.1–0.4, 0.4–2, 2–6, and 6–10 μm splits.

The effects of potential host rock contamination, especially in relatively low-temperature fault rocks formed at the expense of sedimentary rocks and containing significant amounts of illite derived from the sedimentary history of the faulted lithology, are generally assessed with the Illite Age Analysis (IAA) approach (e.g., Hunziker et al., 1986; Peaver, 1999). The IAA discriminates between the mostly detrital $2M_1$ polytype (which in turn might represent a mixture of authigenic high-temperature illite and cataclastic, synkinematic muscovite) and a truly authigenic phase $1M_d$ formed during brittle faulting. To estimate the age and uncertainty of authigenic/synkinematic illite-$1M_d$ and detrital illite-$2M_1$, we normalized to 100% the proportion of illite-$2M_1$ and illite-$1M_d$ determined by X-ray diffraction analysis plotting the data as apparent K-Ar date versus percent of detrital illite, and linearly extrapolated to 0% and 100% illite-$2M_1$ (Figure 6a) by ordinary least square regression. Although more sophisticated regression methods exist which account for the

Table 4
K-Ar Data for the Vallès-Penedès Fault

Sample ID	Grain size fraction (μm)	K (wt %)	Error (%)	Mass rad. ^{40}Ar (mg)	Rad. ^{40}Ar (mol/g)	Error (%)	Rad. ^{40}Ar (%)	Age (Ma)	Error (Ma)
LA73	<0.1	5.696	1.2	3.114	1.062E-09	0.32	81.552	104.5	1.3
	0.1–0.4	5.787	1.2	3.856	1.727E-09	0.31	90.501	164.4	2.0
	0.4–2	5.799	1.2	4.166	2.311E-09	0.31	95.492	216.3	2.6
	2–6	5.087	1.2	4.132	2.615E-09	0.31	98.569	274.5	3.5
	6–10	4.737	1.3	3.032	2.525E-09	0.32	98.668	283.8	3.7
LA74	<0.1	5.565	1.3	4.774	1.993E-09	0.30	89.198	195.5	2.7
	0.1–0.4	5.749	1.2	4.212	2.678E-09	0.31	94.418	250.5	3.1
	0.4–2	5.236	1.2	3.492	2.883E-09	0.31	96.939	292.5	3.7
	2–6	3.465	1.4	4.830	2.093E-09	0.30	98.355	318.5	4.5
	6–10	2.730	1.5	2.874	1.625E-09	0.33	98.540	314.3	4.7
LA76	<0.1	3.531	2.1	5.346	1.280E-09	0.30	83.305	197.9	4.1
	0.1–0.4	4.383	1.3	3.386	2.074E-09	0.32	92.695	254.1	3.4
	0.4–2	4.807	1.3	5.130	2.679E-09	0.30	96.420	295.5	3.8
	2–6	4.312	1.3	3.280	2.593E-09	0.32	98.010	317.2	4.2
	6–10	3.680	1.3	2.802	2.220E-09	0.33	98.090	318.1	4.4
FV11	<0.1	5.027	1.2	3.672	9.167E-10	0.32	75.707	102.2	1.3
	0.1–0.4	5.008	1.2	4.374	1.314E-09	0.31	85.490	145.4	1.9
	0.4–2	4.475	1.3	4.150	1.457E-09	0.31	90.068	178.6	2.3
	2–6	3.135	1.4	3.356	1.014E-09	0.32	90.920	177.5	2.6
	6–10	2.420	1.5	5.176	8.475E-10	0.30	91.057	191.5	2.9

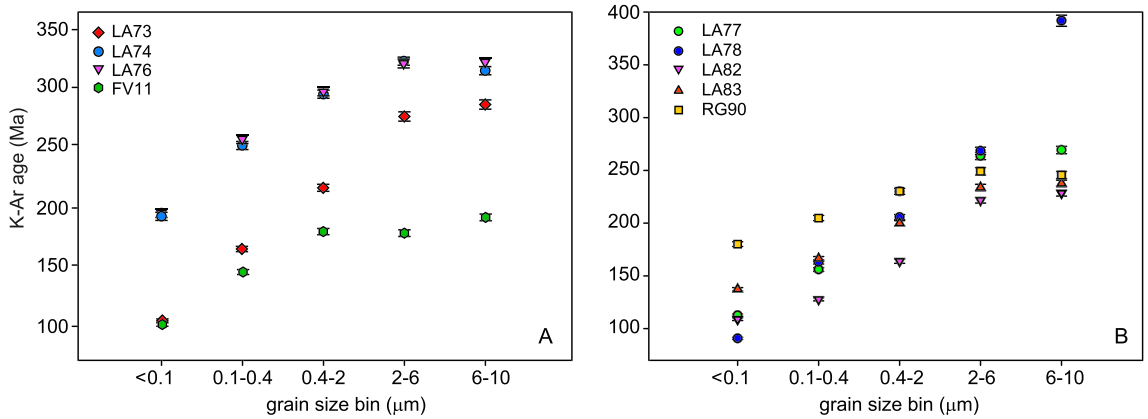

Figure 5. K-Ar age versus grain size spectra for the Vallès-Penedès (a) and Río Grío (b) Faults.

uncertainties on the individual data points (e.g., York et al., 2004), these assume a Gaussian distribution of the uncertainty envelopes in both *x* and *y* coordinates which are likely not valid for the quantified X-ray diffraction mineralogy proportions. By means of this ordinary least square regression, the age of the last slip event recorded by LA73 is at 80 ± 15 Ma, by LA74 at 157 ± 18 Ma, by LA76 at 169 ± 42 Ma, and, finally, by FV11 at 47 ± 18 Ma. Differences between the extrapolated results for the 100% authigenic/synkinematic illite-1M_d and the K-Ar date of the finest <0.1 μm fractions confirm that even the finest separates yield mixed K-Ar dates that have to be considered as maximum ages of faulting. The IAA age of the illite-2M_1 polytype recorded by LA73 is at 284 ± 10 Ma, by LA74 at 318 ± 9 Ma, by LA76 at 320 ± 11 Ma, and, finally, by FV11 at 190 ± 7 Ma. The illite-2M_1 polytype cannot be considered a detrital contamination from the host rocks because the IAA ages are younger than the depositional age of the host rock (Ordovician), and therefore they may record the first (oldest) slip event.

4.3.2. Río Grío Fault

For the Río Grío Fault it was also possible to date five fractions for each of the studied samples thus generating a significant database. Results are shown in Table 5 and illustrated in Figure 5b.

As for the Vallès-Penedès Fault, there is a clear direct grain size-age correlation, with ages becoming progressively younger with decreasing grain size (Figure 5b). For sample LA77, the <0.1 μm fraction yields a K-Ar date of 112.6 ± 1.3 Ma, the 0.1–0.4 μm fraction a date of 156.0 ± 1.8 Ma, the 0.4–2 μm fraction a date of 205.7 ± 2.4 Ma, the 2–6 μm fraction a date of 263.6 ± 3.3 Ma, and, finally, the 6–10 μm split a date of 269.4 ± 3.5 Ma.

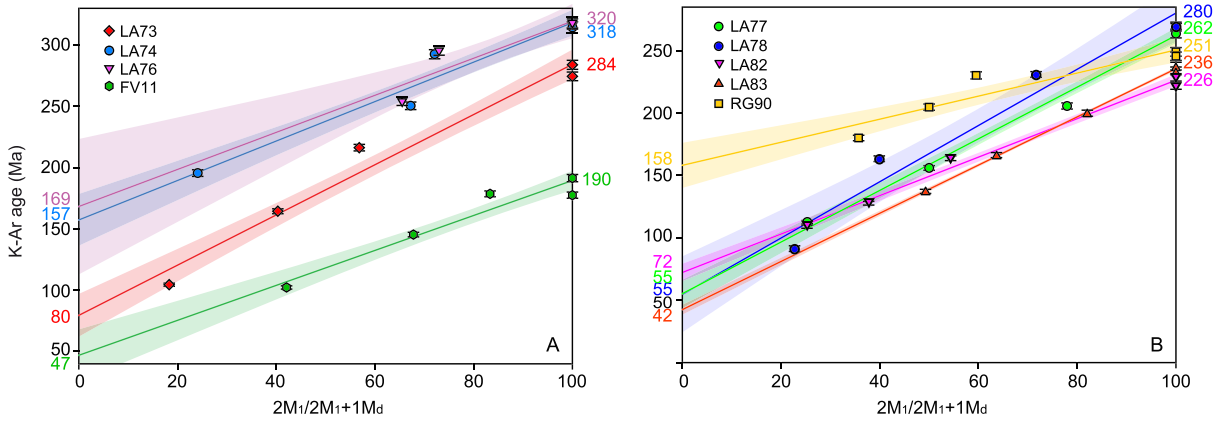

Figure 6. Illite age analysis for the clay gouges of the Vallès-Penedès (a) and Río Grío (b) Faults. To estimate the ages of the authigenic illite-1M_d end-member, which correspond to the last faulting event recorded by the illite, we plotted K-Ar ages versus percentage of illite-2M_1 (normalized to 100%) and linearly extrapolate to 0% illite-2M_1. K-Ar ages extrapolated to 100% illite-2M_1 correspond to the age of the oldest faulting event or represent a detrital component from the host rock (see text).

Table 5
K-Ar Data for the Río Grío Fault

Sample ID	Grain size fraction (μm)	K (wt %)	Error (%)	Mass rad. ^{40}Ar (mg)	Rad. ^{40}Ar (mol/g)	Error (%)	Rad. ^{40}Ar (%)	Age (Ma)	Error (Ma)
LA77	<0.1	6.640	1.1	7.126	1.338E-09	0.30	88.681	112.6	1.3
	0.1–0.4	6.437	1.1	7.964	1.819E-09	0.30	92.482	156.0	1.8
	0.4–2	6.448	1.2	4.820	2.436E-09	0.30	96.352	205.7	2.4
	2–6	5.179	1.2	4.128	2.549E-09	0.31	98.299	263.6	3.3
	6–10	4.520	1.3	8.530	2.277E-09	0.30	98.331	269.4	3.5
LA78	<0.1	6.082	1.2	3.520	9.817E-10	0.32	88.896	90.8	1.1
	0.1–0.4	5.993	1.2	4.114	1.775E-09	0.31	92.573	163.2	2.0
	0.4–2	5.170	1.2	4.308	2.200E-09	0.31	96.551	230.2	2.9
	2–6	4.870	1.3	3.696	2.445E-09	0.31	98.017	268.5	3.5
	6–10	4.149	1.3	2.468	3.148E-09	0.33	98.113	391.8	5.3
LA82	<0.1	7.215	1.1	2.516	1.404E-09	0.34	95.071	108.9	1.3
	0.1–0.4	7.157	1.1	5.234	1.642E-09	0.30	96.563	127.7	1.5
	0.4–2	7.133	1.1	2.748	2.121E-09	0.33	97.777	163.8	1.9
	2–6	6.275	1.2	4.008	2.567E-09	0.31	98.883	221.7	2.7
	6-10	5.828	1.2	5.020	2.461E-09	0.30	98.414	228.5	2.8
LA83	<0.1	6.315	1.2	3.568	1.561E-09	0.31	90.887	137.3	1.6
	0.1–0.4	6.207	1.2	4.500	1.875E-09	0.31	95.033	166.3	2.0
	0.4–2	5.887	1.2	5.384	2.158E-09	0.30	97.100	199.9	2.4
	2–6	4.417	1.3	5.978	1.912E-09	0.30	98.757	233.8	3.1
	6–10	4.557	1.3	5.746	2.007E-09	0.30	98.598	237.7	3.1
RG90	<0.1	5.820	1.2	4.380	1.910E-09	0.31	79.356	180.0	2.2
	0.1–0.4	5.760	1.2	4.930	2.166E-09	0.30	86.711	204.8	2.5
	0.4–2	5.385	1.2	5.940	2.293E-09	0.30	91.677	230.2	2.9
	2–6	3.570	1.4	7.412	1.653E-09	0.30	90.802	249.1	3.5
	6–10	3.916	1.3	3.680	1.786E-09	0.31	91.265	245.6	3.3

Sample LA78 yielded K-Ar dates of 90.8 ± 1.1 Ma, 163.2 ± 2.0 Ma, 230.2 ± 2.9 Ma, 268.5 ± 3.5 Ma, and 391.8 ± 5.3 Ma for the <0.1, 0.1–0.4, 0.4–2, 2–6, and 6–10 μm splits, respectively. Sample LA82 yielded K-Ar dates of 108.9 ± 1.3 Ma, 127.7 ± 1.5 Ma, 163.8 ± 1.9 Ma, 221.7 ± 2.7 Ma, and 228.5 ± 2.8 Ma for the <0.1, 0.1–0.4, 0.4–2, 2–6, and 6–10 μm fractions, respectively. The finest fraction of LA83 yielded a date of 137.3 ± 1.6 Ma, whereas dates of 166.3 ± 2.0 Ma, 199.9 ± 2.4 Ma, 233.8 ± 3.1 Ma, and 237.7 ± 3.1 Ma were obtained from the 0.1–0.4, 0.4–2, 2–6, and 6–10 μm splits, respectively. Finally, sample RG90 yielded K-Ar dates of 180.0 ± 2.2 Ma, 204.8 ± 2.5 Ma, 230.2 ± 2.9 Ma, 249.1 ± 3.5 Ma, and 245.6 ± 3.3 Ma from the finest to the coarsest fractions.

The IAA regression analyses yield 100% authigenic/synkinematic illite-$1M_d$ ages of 55 ± 10 Ma for LA77, 55 ± 23 Ma for LA78, 72 ± 6 Ma for LA82, 42 ± 3 Ma for LA83, and, finally, 158 ± 15 Ma for RG90 (Figure 6b).

The age of the regressed illite-$2M_1$ polytype recorded by LA77 is at 262 ± 5 Ma, by LA78 at 280 ± 18 Ma, by LA82 at 226 ± 4 Ma, by LA83 at 236 ± 1 Ma, and, finally, by RG90 at 251 ± 8 Ma (Figure 6b). The illite-$2M_1$ polytype represents a detrital contamination from the host rocks for samples LA78 and LA83 and an authigenic/synkinematic phase for samples LA77, LA82, and RG90 as IAA ages are older and younger than the depositional age of the host rock, respectively.

5. Discussion

5.1. Multiple Fault Reactivation Episodes Since Post-Variscan Time and Implications for the Iberian Plate Evolution

There is a growing consensus that the K-Ar dates of the <0.1 μm (or finer) illite fraction from a fault gouge most closely match the timing of the last episode of deformation recorded by the fault rock through the growth of synkinematic and authigenic illite (e.g., Boles et al., 2018; Rahl et al., 2011; Solum et al., 2005; Viola et al., 2016).

The polytype of the newly formed illite reflects mostly the thermal boundary conditions, with $1M_d$ being representative of lower-temperature and $2M_1$ of higher-temperature conditions (e.g., Torgersen et al.,

2014). The age of the coarsest fractions can instead be interpreted as an inherited contribution to the fault rock from the host rock, or alternatively and under certain conditions, it may also record an earlier deformation or thermal event (Scheiber & Viola, 2018; Torgersen et al., 2014; Viola et al., 2013, 2016, 2018). The coarsest fractions are thus in general predominantly characterized by mica or illite-$2M_1$ derived from a previous cooling history of the rock or from an earlier faulting or fluid flow/alteration episode. The ages of the intermediate size fractions are more difficult to interpret as they represent mixing between these two end-members.

The plots of age versus grain size (Peaver, 1999) of Figures 5a and 5b are characterized by the presence of some (sub)plateaus (i.e., where the ages of at least two fractions are the same or very similar within error) at either the lower and higher ends of the mixing lines defining the spectra. This is an intermediate situation toward a flat age spectrum wherein all grain size fractions yield the same age (e.g., Torgersen et al., 2015; see also Viola et al., 2016). However, this is a rare scenario for illite from brittle fault rocks, and when illite synkinematic authigenesis can be documented, it argues for a very significant authigenesis during faulting such that illite of the same age can grow in all of the separated and dated grain size fractions, up to 10 μm. In multigrain size fraction analysis of brittle fault rocks, the K-Ar date of the finest fraction is thus considered to be the closest to the age of the last recorded faulting episode, when synkinematic illite growth is instead limited to the finest fraction. Even for the latter, however, the date of the finest fraction might still be "mixed," that is, it still partially reflects the isotopic contribution of K-bearing phases that are not synkinematic but are simply reworked from the host into the fault rock during cataclastic deformation.

The IAA approach can be of significant help in discriminating the net contribution to the final age of the fraction of authigenic/synkinematic illite and of that derived from the earlier rock history (which can also be that of an earlier faulting episode). All samples analyzed in this study permitted calculating the IAA, allowing us to extrapolate "ideal" fully authigenic/synkinematic illite-$1M_d$ and illite-$2M_1$ ages. In the following, we analyze the IAA results and propose interpretative scenarios capable of assigning our results to geologically meaningful tectonic events.

The illite-$2M_1$ IAA ages in the plots of Figures 6a and 6b indicate two main events of illite/muscovite formation during the Carboniferous and Permian for the Vallès-Penedès Fault and during the Late Permian and Late Triassic for the Río Grío Fault. Only the illite-$2M_1$ IAA age from sample FV11 indicates an Early Jurassic crystallization event. The illite/muscovite-$2M_1$ of the coarse fractions cannot be considered as a detrital contribution to the fault rock from the host rock as their K-Ar dates are younger than the depositional age of the host rock themselves. Therefore, the illite populations in the coarse grain size fractions for both faults crystallized authigenically/synkinematically during episodes of regional deformation or fluid flow.

Following the Variscan orogeny, an important period of magmatism related to the subduction of oceanic crust took place in the Catalan Costal Range (Solé et al., 1998). The intrusion of large plutonic bodies and related hypabyssal dykes caused contact metamorphism up to pyroxene-hornfels facies conditions at the end of Carboniferous or during the Permian (Solé et al., 1998). The Vallès-Penedès Fault likely played a role at that time, possibly accommodating isostatic instabilities induced by the emplacement of the magmatic bodies (Figure 7). Evidence of extensional tectonic activity might be recorded by the $2M_1$-IAA age of the coarse fractions that indicate a short time deformation interval (320 ± 11–318 ± 9 Ma, Figure 7). After this tectonic episode associated with Late Variscan magmatism, a second reactivation took place during the Permian as indicated by the $2M_1$-IAA age of 284 ± 10 Ma (Figures 6a and 7) that coincides with the main stage of Variscan post-orogenic extensional faulting (Lago et al., 2004a, b) and the onset of cooling of the Catalan Coastal batholith dated by biotite K-Ar ages to 284 ± 4 Ma (Solé et al., 1998). Illite/muscovite-$2M_1$ IAA ages from the Río Grío Fault (262 ± 5, 251 ± 8, and 226 ± 4 Ma) allow us to propose a longer post-orogenic Variscan evolution for the Iberian Plate than previously assumed. Extensional deformation would extend through Late Triassic times, suggesting a continuity between Permian tectonics/magmatism, where strike-slip faulting played a relevant role (Cantarelli et al., 2013) and Triassic extension/magmatism (Figures 6b and 7; Pocoví et al., 1990).

Evidence of Early Jurassic extensional tectonic activity of the Vallès-Penedès Fault might be recorded by the 190 ± 7 Ma $2M_1$-IAA age (Figure 7), which can be linked to the broader Latest Triassic-Early Jurassic thermotectonic event related to the opening of the Central Atlantic Rift. This event has been constrained by geological evidence in the Catalan Coastal Range, where mafic intrusions, volcanic rocks, and widespread

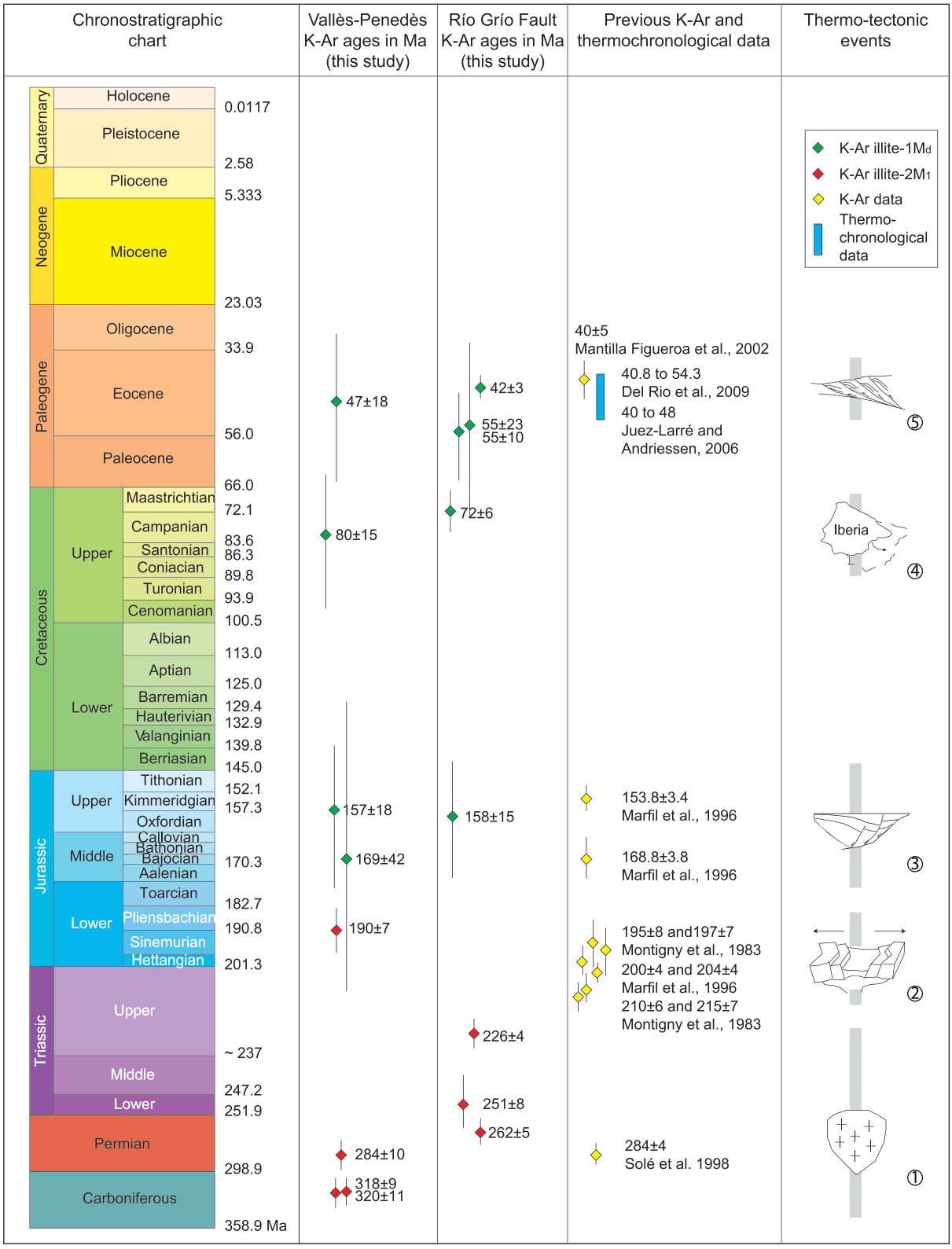

Figure 7. Polyphase activity of the Vallès-Penedès and Río Grío Faults as constrained by the interpretation of our new K-Ar dates and their comparison with previous K-Ar and low-temperature thermochronological data. (1) Post-orogenic extensional faulting associated with Late Variscan magmatism; (2) opening of the Central Atlantic Rift; (3) extensional/transtensional faulting that led to the development of Mesozoic Basins in northern Iberia; (4) final stage of Iberian Plate rotation and accommodation of compressional pulses; (5) positive inversion of Mesozoic extensional basins in response to far-field stresses of the Alpine orogeny.

hydrothermal activity occurred at that time and by 200–203 ± 4 Ma K-Ar ages from authigenic illites in the Iberian Chain, which, taken together, are indicative of significant extensional tectonics and volcanism (Marfil et al., 1996).

Other thermochronological studies throughout the Iberian Peninsula support the obtained illite/muscovite-$2M_1$ IAA age. Montigny et al. (1983), for example, studied ophiolites and lavas associated with Triassic sediments in the Pyrenees obtaining K-Ar ages of 195 ± 8 and 197 ± 7 Ma, and 210 ± 6 and 215 ± 7 Ma respectively. $^{40}Ar/^{39}Ar$ dating and paleomagnetic data of tholeiitic basalts and volcanic dykes from Iberia and other sectors of the Central Atlantic magmatic province indicate that magmatism associated with the opening of the Central Atlantic Rift was most intense at about 200 Ma (Sebai et al., 1991).

The authigenic/synkinematic $1M_d$-IAA ages in the plots of Figures 6a and 6b indicate that illite-$1M_d$ formed during three younger thermotectonic events that can be interpreted as the result of multiple fault reactivation episodes since the Middle-Late Jurassic for both the Vallès-Penedès and Río Grío Faults (Figure 7). These ages and their interpretation are supported by the known Mesozoic-Cenozoic evolution of local intraplate basins of the Iberian Plate, which are excellent markers of the large-scale tectonic events of that time in the Iberian Plate (e.g., Bally, 1982; Figure 8a).

The oldest event of formation of illite-$1M_d$, spanning from Bajocian to earliest Kimmeridgian (169–157 Ma; Figures 6a, 6b, and 7), coincides with the beginning of a major phase of rifting in northern Iberia, related to the opening of the western Tethys and the Central Atlantic Ocean, which caused left-lateral movement of the Iberian Plate relative to Eurasia (Jammes et al., 2010; Salas et al., 2001). Transtensional deformation progressively affected the Iberian Plate, developing distinct extensional systems. Associated crustal thinning diminished from the Pyrenean-Basque-Cantabrian domains to the Central Iberian extensional system (Tugend et al., 2015). In this context, this episode of faulting led to the initial development of Mesozoic extensional/-transtensional basins (e.g., Cameros Basin) which host more than 5-km thick sedimentary sequences (Figure 8a). The timing of this faulting event is consistent with the neoformation of hairy illites in Permian-Triassic red sandstones of the Iberian Chain as a consequence of significant extensional tectonics and fluid circulation that yielded similar K-Ar ages 153.8 ± 3.4 and 168.8 ± 3.8 Ma (Marfil et al., 1996).

A second episode of nucleation of illite-$1M_d$ occurred in the Campanian (80–72 Ma; Figures 6a and 6b) and can be explained within the framework of the rotation of the Iberian Plate. The opening of the North Atlantic during Aptian-Cenomanian times caused 35° anticlockwise rotation of the Iberian Plate with respect to Eurasia (Ziegler et al., 2001). Rotation slowed down during the Latest Cretaceous as a result of the ensuing collision within the context of the Alpine orogeny. The Campanian age suggests fault reactivation in both the Iberian Chain and Catalan Coastal Range as a response to the final stage of plate rotation and the accommodation of the first Pyrenean compressional pulses. The Late Cretaceous tectonics of the Vallès-Penedès Fault is difficult to recognize in the field due to the lack of good outcrops of Cretaceous deposits. The fault zone roughly delimits a southern zone where Mesozoic (Triassic, Jurassic, and, to a lesser extent, Lower Cretaceous) rocks overlie the Paleozoic sediments and igneous rocks, from a northern domain where only Paleozoic low-grade metasediments and Late Variscan granitoids are exposed (Marín et al., 2008; Roca, 1994). The Río Grío Fault neither shows evidence of activity during this period of time, because most sediments of Late Cretaceous age crop out south and west of the studied area. Only some indirect constraints, such as particular fracture patterns (Maestro, 1999) and thickness changes of Cretaceous rocks (Soria de Miguel, 1997), can account for fault activity at that time.

The last documented episode of crystallization of illite-$1M_d$ occurred in the Eocene (approximately 47 Ma for the Vallès-Penedès Fault and between 42 and 55 Ma for the Río Grío Fault) and can be interpreted as due to the far-field stresses of the Alpine orogeny. Intraplate compressional stresses inverted Mesozoic extensional basins in the Iberian Plate during the Paleogene, leading to the development of the Pyrenees, the Iberian Chain, the Spanish Central System, and the Catalan Coastal Range (Casas-Sainz & Faccenna, 2001; Fernández-Lozano et al., 2011; Guimerá & Alvaro, 1990). The Río Grío Fault played a major role during that time, with important transpression documented by the present-day geometry of the Cameros Basin, where Cenozoic compressional structures strike E-W to NW-SE and the footwall of the main thrust consists of up to 4 km thick Eocene molasse of the Ebro Basin (Muñoz-Jiménez & Casas-Sainz, 1997). Furthermore, the reactivation of the Río Grío Fault during the Eocene is supported by a 40 ± 5 Ma K-Ar illite date (Mantilla Figueroa et al., 2002) and by apatite (U-Th)/He and fission-track data indicating that the main part of the

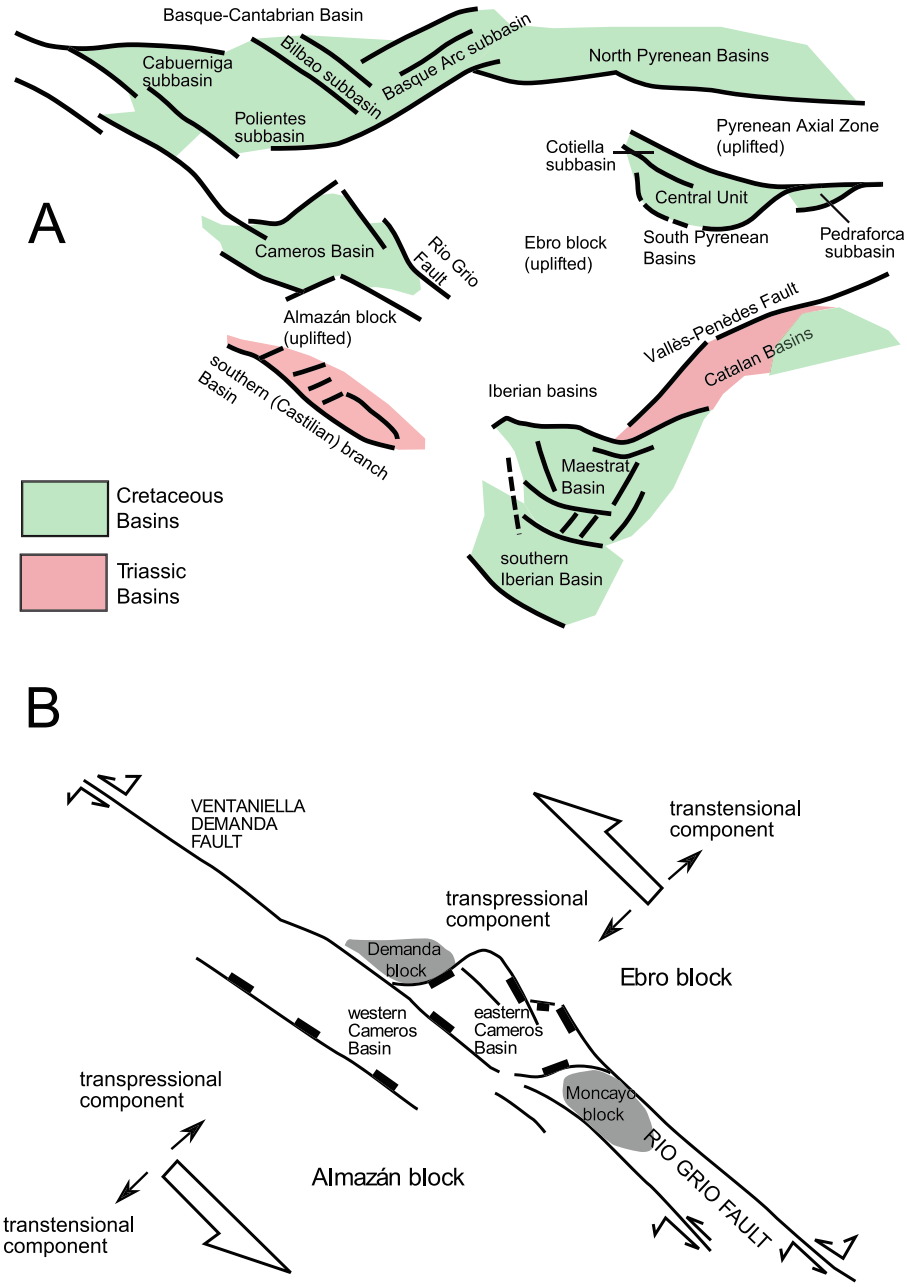

Figure 8. (a) Sedimentary basins and structures in northern Iberia. Río Grío Fault, Vallès-Penedès Fault, Iberian, Catalan, Basque-Cantabrian, and Pyrenean Basins. (b) Interpretation of the Cameros Basin within the frame of northern Iberia and main structures active during basin formation (probably the Río Grío Fault).

Cameros Basin was exhumed at 40 Ma (Del Río et al., 2009). The crystallization of illite-$1M_d$ in the clay gouge of the Vallès-Penedès Fault at about 47 Ma is coeval to the exhumation of a few Variscan granitoids in the Catalan Coastal Range that provided a time interval of 40–48 Ma based on low-temperature thermochronological data (Juez-Larré & Andriessen, 2006). According to these data, there is no clear evidence for diachronous exhumation between the eastern and central parts of the Iberian Peninsula.

5.2. Evidence of Mesozoic Strike-Slip Faulting in Iberia and Switch From Transtensional to Transpressional Regime

The Río Grío Fault can be directly related to the evolution of the Cameros Basin because the multiple movements of the fault fit well temporally important stages of the basin evolution, such as, for example, the

Jurassic-Early Cretaceous rifting, the final stage of the anticlockwise rotation of the Iberian Plate, and the accommodation of compressional pulses that led to the positive inversion of the basin (Figure 7). Sinistral movements along the Río Grío Fault during the Late Cretaceous could represent the response of the plate interior to the anticlockwise rotation of Iberia, within an overall change of the faulting regime from transtension to transpression, as documented in other basins of the northern plate margin (Figure 8a).

Cleavage and low-grade metamorphism in the Cameros Basin have been documented by chloritoid formation, remagnetization (Casas et al., 2009; García-Lasanta et al., 2017; Villalaín et al., 2003), thermal maturity of organic matter (Omodeo-Salé et al., 2017), fluid inclusions (Mata et al., 2001), mineralogy (González-Acebrón et al., 2011; Mata et al., 2001), and fission-track data (Del Río, 2009; Rat et al., 2019). The absolute dating of the thermal metamorphic peak by $^{40}Ar/^{39}Ar$ dating of illite (Goldberg et al., 1988) and K-Ar analysis of illite (Casquet et al., 1992) indicates an age ranging between 86 and 108 Ma. The Albian-Coniacian thermal event, evidenced by a plethora of organic and inorganic thermal and thermochronological indicators, has not been recorded by K-Ar dating of fault gouge indicating that metamorphism postdates the main extensional/transtensional activity of the Río Grío Fault.

The abnormally high-thermal gradient found in the Cameros Basin is thus consistent with a pull-apart basin geometry with master faults that would be striking NW-SE, the Río Grío Fault being the northeastern and the Ventaniella-Demanda Fault (Colchen, 1974; Lepvrier & Martínez-García, 1990; Marcos, 1979) the southwestern (Figure 8b). The scarcity of seismic data prevents us from unequivocally establishing the continuity between the Ventaniella and Demanda fault systems under the Cenozoic fill of the Ebro basin. Nevertheless, their similar strike and the alignment of their mapped traces after restoring the Cenozoic convergent movement between the Southern Pyrenees and the Cameros-Demanda Massif, point to their initial physical continuity, such that they can be assigned to a single fault system. Sinistral movement along the Ventaniella-Demanda and Río Grío Faults would form a tensional jog, thus providing the possibility of strong subsidence and crustal thinning. Transtension could also steer the geometry of normal faults at the northern basin border, the most active during the basinal stage (Casas et al., 2009; Villalaín et al., 2003). Within this tectonic frame, the early inversion interpreted from the sedimentary geometry of the basin filling or foliation development (Soto, Casas-Sainz, et al., 2008) can be explained by a switch from transtension to transpression following a small change of the movement vector of Iberia with respect to Eurasia, always keeping a generalized sinistral displacement approximately parallel to the North Pyrenean transform (as defined by Choukroune et al., 1973).

5.3. Implications for Long-Term Fault Activity and Reactivation

The first K-Ar dating of illite-bearing gouges in northern Iberia permits the following important considerations:

1. The episodes of faulting of the studied long-lived faults are not easy to constrain and are more complicated than previously thought and described in the literature (Casas-Sainz & Gil-imaz, 1998; Villalaín et al., 2003). Syn-tectonic sedimentation, biostratigraphy of continental deposits, hydrothermal mineralizations, and kinematic indicators may partly assist when unraveling the long-term evolution of fault zones but may be insufficient for unraveling multiple reactivations and long slip histories. K-Ar dating of fault gouges and illite polytype determinations proved to be a valuable tool for unraveling extremely complex fault architectures and single out the key thermotectonic stages of intraplate brittle deformation. These new absolute age constraints need to be considered for further tectonic and geodynamic reconstructions.
2. K-Ar dating of fault gouges is sensitive to P-T conditions at which brittle deformation occurs. The fault rocks of the Río Grío and Vallès-Penedès Faults did not yield K-Ar dates younger than the Eocene, even though Alpine deformation is documented until the Late Miocene for some areas of the Iberian Chain and the Middle Miocene for the Catalan Coastal Range. Sedimentological, structural, and low-temperature thermochronological studies for the latter range showed that rocks exposed nowadays were deformed at a maximum depth of 3.6 km during the Paleogene compression at a temperature of 110 °C, and they were at depths of about 2 km and temperatures lower than 60 °C prior to the Miocene extension (Anadón et al., 1979; Cantarero et al., 2014; Juez-Larré & Andriessen, 2006). This may suggest that Late Oligocene-Miocene deformation in both chains occurred under shallower and/or cooler P-T conditions than those prevailing during Mesozoic and Eocene times and/or the absence of physicochemical conditions favorable to illite authigenic growth during brittle deformation.

3. Reactivation of fault zones does not necessarily correspond to the timing of the highest temperature thermal event. K-Ar dating of gouges from the Río Grío Fault does not record the Albian-Coniacian thermal peak in the Cameros Basin, indicating that metamorphism postdates the main extensional/transtensional activity of the Río Grío Fault. This stresses the need of a truly multidisciplinary study when aiming at unraveling the details of complex and long lasting intraplate faulting.

6. Conclusions

K-Ar dating of illite from clay gouges of crustal-scale faults of NE Iberia sheds new light onto the polyphase tectonic activity of the Río Grío and Vallès-Penedès Faults, two major structures that played a significant role in the development and subsequent shaping of Mesozoic and Cenozoic sedimentary basins of the Iberian Plate. Illite/muscovite-$2M_1$ K-Ar ages indicated that faulting was coeval to Late Variscan hydrothermal mineralizations and magmatism and suggest a longer Variscan post-orogenic evolution for the Iberian Plate than thought earlier, extending the period of extensional tectonics until the Late Triassic, as, for example, the prolonged, discontinuous magmatic activity found by former authors seem to indicate.

Authigenic/synkinematic illite-$1M_d$ dates indicate multiple fault reactivations in response to the known key stages of the thermotectonic evolution of the Iberian Plate. Faults were reactivated during the Late Jurassic-Early Cretaceous rifting that led to the development of Mesozoic extensional/transtensional basin in northern Iberia, in Campanian time as a consequence of final stage of plate rotation, and during the compressional pulses associated with the Alpine orogeny (Paleogene). The results obtained from these two well-constrained examples of the Iberian Plate confirm that crustal-scale faults can indeed be reactivated under a variety of tectonic contexts and that thermotectonic conditions characterized by high-geothermal gradients strongly favor fault movement and neoformation of clay minerals in fault gouges, regardless of the prevailing tectonic regime (compressional, extensional, or strike-slip).

Acknowledgments
This work was supported by Project CGL-2013-42670-P and a pre-doctoral grant to Marcos Marcén from the Spanish Ministry of Science and Education. Financial support from Progetti di Ateneo 2018 and FFABR 2017 to Luca Aldega is acknowledged. Ruikai Xie and Clea Fabian from the Geological Survey of Norway are thanked for assistance with K analysis and sample preparation. We are grateful to Peter van der Beek, Gerardo de Vicente, and Jeffrey Rahl for detailed revisions and helpful suggestions. X-ray and K-Ar geochronological data can be accessed via the following URL: https://doi.org/10.1594/IEDA/111380, checking the dataset by Aldega et al. (2019).

References

Aldega, L., Corrado, S., Grasso, M., & Maniscalco, R. (2007). Correlation of diagenetic data from organic and inorganic studies in the Apenninic-Maghrebian fold-and-thrust belt: A case study from Eastern Sicily. *The Journal of Geology*, *115*(3), 335–353. https://doi.org/10.1086/512756

Aldega, L., Viola, G., Casas-Sainz, A., Marcén, M., Román-Berdiel, T., & van der Lelij, R. (2019). X-ray diffraction and K-Ar geochronological data of fault rocks in northern Iberia. *Interdisciplinary Earth Data Alliance (IEDA)*. https://doi.org/10.1594/IEDA/111380

Alvaro, M., Capote del Villar, R., & Vegas, R. (1979). Un modelo de evolución geotectónica para la Cadena Celtibérica. *Acta Geologica Hispánica*, *14*(1), 172–177.

Anadón, P., Colombo, F., Esteban, M., Marzo, M., Robles, S., Santanach, P., & Sugrañes, S. (1979). Evolución tectonoestratigráfica de los Catalánides. *Acta Geologica Hispánica*, *14*, 242–270.

Antolín-Tomás, B., Liesa, C. L., Casas, A. M., & Gil-Peña, I. (2007). Geometry of fracturing linked to extension and basin formation in the Maestrazgo basin (Eastern Iberian Chain, Spain). *Revista de la Sociedad Geológica de España*, *20*(3-4), 351–365.

Arthaud, F., & Matte, P. (1977). Late Paleozoic strike-slip faulting in southern Europe and northern Africa: Result of a right-lateral shear zone between the Appalachians and the Urals. *Geological Society of America Bulletin*, *88*(9), 1305–1320. https://doi.org/10.1130/0016-7606(1977)88<1305:LPSFIS>2.0.CO;2

Bally, A. W. (1982). Musings over sedimentary basin evolution. *Philosophical Transactions of the Royal Society A*, *305*(1489), 325–338. https://doi.org/10.1098/rsta.1982.0040

Boles, A., Schleicher, A. M., Solum, J., & van der Pluijm, B. A. (2018). Quantitative X-ray powder diffraction and the illite polytype analysis method for direct fault rock dating: A comparison of analytical techniques. *Clays and Clay Minerals*, *66*, 220–232.

Calvín-Ballester, P., & Casas, A. (2014). Folded Variscan thrusts in the Herrera unit of the Iberian Range (NE Spain). *Geological Society, London, Special Publications*, *394*(1), 39–52. https://doi.org/10.1144/SP394.3

Canals, À., & Ayora, C. (1988). Las mineralizaciones filonianas del sector de l'Argentera (Cadenas Costeras Catalanas): contexto geológico, estructura, tipología y condiciones de formación. *Acta Geologica Hispánica*, *23*(3), 155–170.

Canals, A., & Cardellach, E. (1997). Ore lead and sulphur isotope pattern from the low temperature veins of the Catalonian Coastal Ranges (NE Spain). *Mineralium Deposita*, *32*(3), 243–249. https://doi.org/10.1007/s001260050089

Cantarelli, V., Aldega, L., Corrado, S., Invernizzi, C., & Casas-Sainz, A. (2013). Thermal history of the Aragón-Béarn basin (Late Paleozoic, western Pyrenees, Spain); insights into basin tectonic evolution. *Italian Journal of Geosciences*, *132*(3), 443–462. https://doi.org/10.3301/IJG.2012.41

Cantarero, I., Lanari, P., Vidal, O., Alías, G., Travé, A., & Baqués, V. (2014). Long-term fluid circulation in extensional faults in the central Catalan Coastal Ranges: P–T constraints from neoformed chlorite and K-white mica. *International Journal of Earth Sciences*, *103*(1), 165–188. https://doi.org/10.1007/s00531-013-0963-8

Casas, A. M., Villalaín, J. J., Soto, R., Gil-Imaz, A., del Río, P., & Fernández, G. (2009). Multidisciplinary approach to an extensional syncline model for the Mesozoic Cameros Basin (N Spain). *Tectonophysics*, *470*(1-2), 3–20. https://doi.org/10.1016/j.tecto.2008.04.020

Casas Sainz, A. M. (1993). Oblique tectonic inversion and basement thrusting in the Cameros Massif (Northern Spain). *Geodinamica Acta*, *6*(3), 202–216. https://doi.org/10.1080/09853111.1993.11105248

Casas-Sainz, A., & Faccenna, C. (2001). Tertiary compressional deformation of the Iberian plate. *Terra Nova*, *13*(4), 281–288. https://doi.org/10.1046/j.1365-3121.2001.00355.x

Casas-Sainz, A. M., & Gil-imaz, A. (1998). Extensional subsidence, contractional folding and thrust inversion of the Eastern Cameros Basin, Northern Spain. *Geologische Rundschau*, *86*(4), 802–818. https://doi.org/10.1007/s005310050178

Casas-Sainz, A. M., Gil-Imaz, A., Simón, J. L., Izquierdo-Llavall, E., Aldega, L., Román-Berdiel, T., et al. (2018). Strain indicators and magnetic fabric in intraplate fault zones: Case study of Daroca thrust, Iberian Chain, Spain. *Tectonophysics*, *730*, 29–47. https://doi.org/10.1016/j.tecto.2018.02.013

Casas-Sainz, A. M., Román-Berdiel, T., Oliva-Urcia, B., García-Lasanta, C., Villalaín, J. J., Aldega, L., et al. (2017). Multidisciplinary approach to constrain kinematics of fault zones at shallow depths: A case study from the Cameros–Demanda thrust (North Spain). *International Journal of Earth Sciences*, *106*(3), 1023–1055. https://doi.org/10.1007/s00531-016-1349-5

Casquet, A., Galindo, C., González-Casado, J. M., Alonso, A., Mas, R., Rodas, M., et al. (1992). El metamorfismo en la cuenca de los Cameros. *Geocronología e implicaciones tectónicas. Geogaceta*, *11*, 22–25.

Choukroune, P., Seguret, M., & Galdeano, A. (1973). Caracteristiques et evolution structurale des Pyrenees; un modele de relations entre zone orogenique et mouvement des plaques. *Bulletin de la Société géologique de France*, *7*(5-6), 600–611.

Colchen, M. (1974). *Geologie de la Sierra de la Demanda* (Vol. 85). Burgos-Logroño (Espagne): Memoria del Instituto Geológico y Minero de España.

Cortés, A. L., Liesa, C. L., Soria, A. R., & Meléndez, A. (1999). Role of extensional structures on the location of folds and thrusts during tectonic inversion (northern Iberian Chain, Spain). *Geodinamica Acta*, *12*(2), 113–132. https://doi.org/10.1080/09853111.1999.11105335

Cortés-Gracia, A. L., & Casas Sainz, A. M. (1996). Deformación alpina de zócalo y cobertera en el borde norte de la Cordillera Ibérica (Cubeta de Azuara-Sierra de Herrera). *Revista de la Sociedad Geológica de España*, *9*(1-2), 51–66.

De Bruijne, C. H., & Andriessen, P. A. M. (2002). Far field effects of Alpine plate tectonism in the Iberian microplate recorded by fault-related denudation in the Spanish Central System. *Tectonophysics*, *349*(1-4), 161–184. https://doi.org/10.1016/S0040-1951(02)00052-5

De Vicente, G. (2018). Geological record of the alpine deformations in Iberia: Strain partitioning or tectonic phases. *Revista de la Sociedad Geológica de España*, *31*(2), 13–22.

De Vicente, G., & Muñoz-Martín, A. (2013). The Madrid Basin and the Central System: A tectonostratigraphic analysis from 2D seismic lines. *Tectonophysics*, *602*, 259–285. https://doi.org/10.1016/j.tecto.2012.04.003

De Vicente, G., Vegas, R., Martín, A. M., Silva, P. G., Andriessen, P., Cloetingh, S., et al. (2007). Cenozoic thick-skinned deformation and topography evolution of the Spanish Central System. *Global and Planetary Change*, *58*(1-4), 335–381. https://doi.org/10.1016/j.gloplacha.2006.11.042

De Vicente, G., Vegas, R., Muñoz-Martín, A., Van Wees, J. D., Casas-Sáinz, A., Sopeña, A., et al. (2009). Oblique strain partitioning and transpression on an inverted rift: The Castilian Branch of the Iberian Chain. *Tectonophysics*, *470*(3-4), 224–242. https://doi.org/10.1016/j.tecto.2008.11.003

Del Río, P. (2009). Historia termal del sector oriental de la Sierra de Cameros: restricciones a partir del análisis de huellas de fisión y otras herramientas geocronológicas (U-Pb SHRIMP y (U-Th/He). PhD, University of Zaragoza

Del Río, P., Barbero, L., & Stuart, F. M. (2009). Exhumation of the Sierra de Cameros (Iberian Range, Spain): Constraints from low-temperature thermochronology. *Geological Society, London, Special Publications*, *324*(1), 153–166.

Doblas, M., López-Ruiz, J., Oyarzun, R., Mahecha, V., Moya, Y. S., Hoyos, M., et al. (1994). Extensional tectonics in the central Iberian Peninsula during the Variscan to Alpine transition. *Tectonophysics*, *238*(1-4), 95–116. https://doi.org/10.1016/0040-1951(94)90051-5

Eberl, D. D., Środoń, J., Lee, M., Nadeau, P. H., & Northrup, H. R. (1987). Sericite from the Silverton caldera, Colorado: Correlation among structure, composition, origin, and particle thickness. *American Mineralogist*, *72*, 914–934.

Fernández-Lozano, J., Sokoutis, D., Willingshofer, E. D., Cloetingh, S., & De Vicente, G. (2011). Cenozoic deformation of Iberia: A model for intraplate mountain building and basin development based on analogue modeling. *Tectonics*, *30*, TC1001. https://doi.org/10.1029/2010TC002719

Fontboté, J. M. (1954). Las relaciones tectónicas de la depresión del Vallés-Penedés con la cordillera prelitoral catalana y con la depresión del Ebro. *Boletín de la Real Sociedad Española de Historia Natural. Sección Geológica*, *52*, 281–310.

Fontboté, J. M., Guimerà, J., Roca, E., Sàbat, F., Santanach, P., & Fernández-Ortigosa, F. (1990). The Cenozoic geodynamic evolution of the Valencia trough (western Mediterranean). *Revista de la Sociedad Geológica de España*, *3*(3-4), 249–259.

García-Lasanta, C., Casas-Sainz, A., Villalaín, J. J., Oliva-Urcia, B., Mochales, T., & Speranza, F. (2017). Remagnetizations used to unravel large-scale fold kinematics: A case study in the Cameros Basin (Northern Spain). *Tectonics*, *36*, 714–729. https://doi.org/10.1002/2016TC004459

Goldberg, J. M., Guiraud, M., Maluski, H., & Séguret, M. (1988). Caractères pétrologiques et âge du métamorphisme en contexte distensif du bassin sur décrochement de Soria (Crétacé inférieur, Nord Espagne). *Comptes Rendus de le Académie des Sciences Paris*, *307*, 521–527.

Gomes, A., Chaminé, H. I., Teixeira, J., Fonseca, P. E., Pereira, L. G., de Jesus, A. P., et al. (2007). Late Cenozoic basin opening in relation to major strike-slip faulting along the Porto–Coimbra–Tomar fault zone (Northern Portugal). In *In Sedimentary processes, environments and basins: A tribute to Peter friend* (pp. 137–153). Oxford, UK: Blackwell Publishing Ltd.

Gong, Z., Langereis, C. G., & Mullender, T. A. T. (2008). The rotation of Iberia during the Aptian and the opening of the Bay of Biscay. *Earth and Planetary Science Letters*, *273*(1-2), 80–93. https://doi.org/10.1016/j.epsl.2008.06.016

Gong, Z., van Hinsbergen, D. J., Vissers, R. L., & Dekkers, M. J. (2009). Early Cretaceous syn-rotational extension in the Organyà basin—New constraints on the palinspastic position of Iberia during its rotation. *Tectonophysics*, *473*(3-4), 312–323. https://doi.org/10.1016/j.tecto.2009.03.003

González-Acebrón, L., Goldstein, R. H., Mas, R., & Arribas, J. (2011). Criteria for recognition of localization and timing of multiple events of hydrothermal alteration in sandstones illustrated by petrographic, fluid inclusion, and isotopic analysis of the Tera Group, Northern Spain. *International Journal of Earth Sciences*, *100*(8), 1811–1826. https://doi.org/10.1007/s00531-010-0606-2

Guimerà, J. (1984). Palaeogene evolution of deformation in the northeastern Iberian Peninsula. *Geological Magazine*, *121*(5), 413–420. https://doi.org/10.1017/S0016756800029940

Guimerá, J., & Alvaro, M. (1990). Structure et évolution de la compression alpine dans la Chaîne Ibérique et la Chaîne côtière catalane (Espagne). *Bulletin de la Société géologique de France*, *6*(2), 339–348.

Hałas, S., & Wójtowicz, A. (2014). Propagation of error formulas for K/Ar dating method. *Geochronometria*, *41*(3), 202–206. https://doi.org/10.2478/s13386-013-0162-1

Hunziker, J. C., Frey, M., Clauer, N., Dallmeyer, R., Friedrichsen, H., Flehmig, W., et al. (1986). The evolution of illite to muscovite: Mineralogical and isotopic data from the Glarus Alpes, Switzerland. *Contributions to Mineralogy and Petrology*, *92*(2), 157–180. https://doi.org/10.1007/BF00375291

Institut Cartogràfic de Catalunya (2005). Mapa geològic comarcal de Catalunya (scale 1:50.000, sheet 13-Barcelonès). Institut Cartogràfic de Catalunya.

Institut Cartogràfic de Catalunya (2006a). Mapa geològic comarcal de Catalunya (scale 1:50.000; sheet 29-Priorat). Institut Cartogràfic de Catalunya.
Institut Cartogràfic de Catalunya (2006b). Mapa geològic comarcal de Catalunya (scale 1:50.000, sheet 34- Selva). Institut Cartogràfic de Catalunya.
Jagodzinski, H. (1949). Eindimensionale Fehlordnung in Kristallen und ihr Einfluss auf die Röntgen Interferenzen. *Acta Crystallographica*, *2*(4), 201–207. https://doi.org/10.1107/S0365110X49000552
Jammes, S., Lavier, L., & Manatschal, G. (2010). Extreme crustal thinning in the Bay of Biscay and the Western Pyrenees: From observations to modeling. *Geochemistry, Geophysics, Geosystems*, *11*, Q10016. https://doi.org/10.1029/2010GC003218
Juárez, M. T., Lowrie, W., Osete, M. L., & Meléndez, G. (1998). Evidence of widespread Cretaceous remagnetisation in the Iberian Range and its relation with the rotation of Iberia. *Earth and Planetary Science Letters*, *160*(3-4), 729–743. https://doi.org/10.1016/S0012-821X(98)00124-1
Juárez, M. T., Osete, M. L., Meléndez, G., Langereis, C. G., & Zijderveld, J. D. A. (1994). Oxfordian magnetostratigraphy of the Aguilón and Tosos sections (Iberian Range, Spain) and evidence of a pre-Oligocene overprint. *Physics of the Earth and Planetary Interiors*, *85*(1-2), 195–211. https://doi.org/10.1016/0031-9201(94)90017-5
Juárez, M. T., Osete, M. L., Vegas, R., Langereis, C. G., & Meléndez, G. (1996). Palaeomagnetic study of Jurassic limestones from the Iberian Range (Spain): tectonic implications. *Geological Society, London, Special Publications*, *105*(1), 83–90. https://doi.org/10.1144/GSL.SP.1996.105.01.07
Juez-Larré, J., & Andriessen, P. A. M. (2006). Tectonothermal evolution of the northeastern margin of Iberia since the break-up of Pangea to present, revealed by low-temperature fission-track and (U–Th)/He thermochronology: A case history of the Catalan Coastal Ranges. *Earth and Planetary Science Letters*, *243*(1-2), 159–180. https://doi.org/10.1016/j.epsl.2005.12.026
Kronberg, P. (1991). Crustal fracturing and intraplate tectonics in the area between the North Sea and the Alps: A comparison of Landsat-derived fractures with existing map data. *Tectonophysics*, *195*(2-4), 261–269. https://doi.org/10.1016/0040-1951(91)90214-D
Lago, M., Arranz, E., Pocoví, A., Galé, C., & Gil-Imaz, A. (2004a). Lower Permian magmatism of the Iberian Chain, Central Spain, and its relationship to extensional tectonics. *Geological Society, London, Special Publications*, *223*(1), 465–490. https://doi.org/10.1144/GSL.SP.2004.223.01.20
Lago, M., Arranz, E., Pocovi, A., Galé, C., & Gil-Imaz, A. (2004b). Permian magmatism and basin dynamics in the southern Pyrenees: A record of the transition from late Variscan transtension to early Alpine extension. *Geological Society, London, Special Publications*, *223*(1), 439–464. https://doi.org/10.1144/GSL.SP.2004.223.01.19
Lee, J.-Y., Marti, K., Severinghaus, J. P., Kawamura, K., Yoo, H.-S., Lee, J. B., & Kim, J. S. (2006). A redetermination of the isotopic abundances of atmospheric Ar. *Geochimica et Cosmochimica Acta*, *70*(17), 4507–4512. https://doi.org/10.1016/j.gca.2006.06.1563
Lepvrier, C., & Martínez-García, E. (1990). Fault development and stress evolution of the post-Hercynian Asturian Basin (Asturias and Cantabria, northwestern Spain). *Tectonophysics*, *184*(3-4), 345–356. https://doi.org/10.1016/0040-1951(90)90447-G
Liesa, C., Casas, A., & Simón, J. L. (2018). Tectónica de inversión en una cadena intraplaca: la Cordillera Ibérica. *Revista de la Sociedad Geológica de España*, *31*(2), 23–50.
Llana-Fúnez, S., & Marcos, A. (2001). The Malpica–Lamego Line: A major crustal-scale shear zone in the Variscan belt of Iberia. *Journal of Structural Geology*, *23*(6-7), 1015–1030. https://doi.org/10.1016/S0191-8141(00)00173-5
Llopis Lladó, N. (1947). Contribución al conocimiento de la morfoestructura de los Catalánides; estudio geológico, 372 pp.
Maestro, A. (1999). Estructura y evolución alpina de la Cuenca de Almazán (Cordillera Ibérica) (Doctoral dissertation, Tesis doctoral. Universidad de Zaragoza).
Malavieille, J. (1993). Late orogenic extension in mountain belts: Insights from the Basin and Range and the late Paleozoic Variscan belt. *Tectonics*, *12*(5), 1115–1130. https://doi.org/10.1029/93TC01129
Mantilla Figueroa, L. C., Galindo, C., Mas, R., & Casquet, C. (2002). El metamorfismo hidrotermal cretácico y paleógeno en la cuenca de Cameros (Cordillera Ibérica, España). *Zubía*, *14*, 143–154.
Marcén, M., Casas-Sainz, A. M., Román-Berdiel, T., Griera, A., Santanach, P., Pocoví, A., et al. (2018). Multiple movements recorded in a crustal weakness zone in NE Iberia: The Vallès-Penedès Fault revisited. *Journal of Geodynamics*, *121*, 96–114. https://doi.org/10.1016/j.jog.2018.07.003
Marcén, M., & Román Berdiel, T. (2015). Geometría y cinemática de la zona de falla de Río Grío: evidencias de transpresión alpina en la Cadena Ibérica. *Geotemas*, *58*, 79–82.
Marcos, A. (1979). Facies differentiation caused by wrench deformation along a deep-seated fault system (León line, Cantabrian Mountains, North Spain)—Discussion. *Tectonophysics*, *60*(3-4), 303–308. https://doi.org/10.1016/0040-1951(79)90168-9
Marfil, R., Bonhomme, M. G., De la Peña, J. A., Penha Dos Santos, R., & Sell, I. (1996). La edad de las ilitas en areniscas pérmicas y triásicas de la cordillera Ibérica mediante el método K/Ar: Implicaciones en la historia diagenética y evolución de la cuenca. *Cuadernos de Geología Ibérica*, *20*, 61–83.
Marín, M. A., Roca, E., Rosell, O., Marcuello, A., & Cabrera, L. (2008). La Falla del Montmell: un ejemplo del control ejercido por las fallas extensivas mesozoicas en la arquitectura cenozoica de las Cadenas Costeras Catalanas. *Geotemas (Madrid)*, *2*, 462–464.
Marques, F. O., Mateus, A., & Tassinari, C. (2002). The Late-Variscan fault network in central–northern Portugal (NW Iberia): A re-evaluation. *Tectonophysics*, *359*(3-4), 255–270. https://doi.org/10.1016/S0040-1951(02)00514-0
Martinez-Peña, M., & Casas-Sainz, A. (2003). Cretaceous–Tertiary tectonic inversion of the Cotiella Basin (southern Pyrenees, Spain). *International Journal of Earth Sciences*, *92*(1), 99–113.
Mata, M. P., Casas, A. M., Canals, A., Gil, A., & Pocovi, A. (2001). Thermal history during Mesozoic extension and tertiary uplift in the Cameros Basin, northern Spain. *Basin Research*, *13*(1), 91–111. https://doi.org/10.1046/j.1365-2117.2001.00138.x
Matthews, K. J., Seton, M., & Müller, R. D. (2012). A global-scale plate reorganization event at 105–100 Ma. *Earth and Planetary Science Letters*, *355*, 283–298.
McDougall, I., & Wellman, P. (2011). Calibration of GA1550 biotite standard for K/Ar and $^{40}Ar/^{39}Ar$ dating. *Chemical Geology*, *280*(1-2), 19–25. https://doi.org/10.1016/j.chemgeo.2010.10.001
Montigny, B., Azambre, B., Rossy, M., & Thuizat, R. (1983). Étude K/Ar du magmatisme basique lié au Trias supérier des Pyrénées—Conséquences méthodologiques et paléogeographiques. *Bulletin de Mineralogie*, *105*, 673–680.
Moore, D. M., & Reynolds, R. C. Jr. (1997). *X-ray diffraction and the identification and analysis of clay minerals* (p. 378). Oxford, UK: Oxford University Press.
Moussaid, B., Villalaín, J. J., Casas-Sainz, A., El Ouardi, H., Oliva-Urcia, B., Soto, R., et al. (2015). Primary vs. secondary curved fold axes: Deciphering the origin of the Aït Attab syncline (Moroccan High Atlas) using paleomagnetic data. *Journal of Structural Geology*, *70*, 65–77. https://doi.org/10.1016/j.jsg.2014.11.004

Muñoz-Jiménez, A., & Casas-Sainz, A. M. (1997). The Rioja Trough (N Spain): Tectosedimentary evolution of a symmetric foreland basin. *Basin Research*, *9*(1), 65–85. https://doi.org/10.1046/j.1365-2117.1997.00031.x

Neres, M., Font, E., Miranda, J. M., Camps, P., Terrinha, P., & Mirão, J. (2012). Reconciling Cretaceous paleomagnetic and marine magnetic data for Iberia: New Iberian paleomagnetic poles. *Journal of Geophysical Research*, *117*, B06102. https://doi.org/10.1029/2011JB009067

Omodeo-Salé, S., Salas, R., Guimerà, J., Ondrak, R., Mas, R., Arribas, J., & Martinez, L. (2017). Subsidence and thermal history of an inverted Late Jurassic-Early Cretaceous extensional basin (Cameros, North-central Spain) affected by very low-to low-grade metamorphism. *Basin Research*, *29*(S1), 156–174. https://doi.org/10.1111/bre.12142

Palencia-Ortas, A., Osete, M. L., Vegas, R., & Silva, P. (2006). Paleomagnetic study of the Messejana Plasencia dyke (Portugal and Spain): A lower Jurassic paleopole for the Iberian plate. *Tectonophysics*, *420*(3-4), 455–472. https://doi.org/10.1016/j.tecto.2006.04.003

Peaver, D. R. (1999). Illite and hydrocarbon exploration. *Proceedings of the National Academy of Sciences USA*, *96*(7), 3440–3446. https://doi.org/10.1073/pnas.96.7.3440

Picha, F. J. (2002). Late orogenic strike-slip faulting and escape tectonics in frontal Dinarides-Hellenides, Croatia, Yugoslavia, Albania, and Greece. *AAPG Bulletin*, *86*(9), 1659–1671.

Pocoví, J. A., Osácar Soriano, M. C., & Lago, M. (1990). Análisis estructural de las mineralizaciones de baritina de la Unidad de Herrera (Cordillera Ibérica Oriental). *Geogaceta*, (8), 25–28.

Rahl, J. M., Haines, S. H., & van der Pluijm, B. A. (2011). Links between orogenic wedge deformation and erosional exhumation: Evidence from illite age analysis of fault rock and detrital thermochronology of syn-tectonic conglomerates in the Spanish Pyrenees. *Earth and Planetary Science Letters*, *307*(1-2), 180–190. https://doi.org/10.1016/j.epsl.2011.04.036

Rat, J., Mouthereau, F., Brichau, S., Crémades, A., Bernet, M., Balvay, M., et al. (2019). Tectonothermal evolution of the Cameros Basin: Implications for tectonics of North Iberia. *Tectonics*, *38*, 440–469. https://doi.org/10.1029/2018TC005294

Renne, P. R., Cassata, W. S., & Morgan, L. E. (2009). The isotopic composition of atmospheric argon and $^{40}Ar/^{39}Ar$ geochronology: Time for a change? *Quaternary Geochronology*, *4*(4), 288–298. https://doi.org/10.1016/j.quageo.2009.02.015

Roca, E. (1994). La evolución geodinámica de la Cuenca Catalano-Balear y áreas adyacentes desde el Mesozoico hasta la actualidad. *Acta Geologica Hispánica*, *29*(1), 3–25.

Roca, E., Sans, M., Cabrera, L., & Marzo, M. (1999). Oligocene to middle Miocene evolution of the central Catalan margin (northwestern Mediterranean). *Tectonophysics*, *315*(1-4), 209–229. https://doi.org/10.1016/S0040-1951(99)00289-9

Román-Berdiel, T., Pueyo-Morer, E. L., & Casas-Sainz, A. M. (1995). Granite emplacement during contemporary shortening and normal faulting: structural and magnetic study of the Veiga Massif (NW Spain). *Journal of Structural Geology*, *17*(12), 1689–1706. https://doi.org/10.1016/0191-8141(95)00062-I

Rosenbaum, G., Lister, G. S., & Duboz, C. (2002). Relative motions of Africa, Iberia and Europe during Alpine orogeny. *Tectonophysics*, *359*(1-2), 117–129. https://doi.org/10.1016/S0040-1951(02)00442-0

Salas, R., Guimerà, J., Mas, R., Martín-Closas, C., Meléndez, A., & Alonso, A. (2001). Evolution of the Mesozoic central Iberian Rift System and its Cainozoic inversion (Iberian chain). In P. A. Ziegler, W. Cavazza, A. H. F. Robertson, & S. Crasquin-Soleau (Eds.), *Peri-Tethys Memoir 6*: Peri-Tethyan Rift/Wrench Basins and Passive Margins (Vol. 186, pp. 145–185). Paris: Mémoires du Muséum national d' Histoire naturelle.

Santanach, P., & Julià, R. (1984). Estructuras en la salbanda de la falla paleogena de la falla del Vallés-Penedés (Cadenas Costeras Catalanas) su relación con el deslizamiento de la falla. I Congreso español de geología, Segovia, 3, 47-60.

Scheiber, T., & Viola, G. (2018). Complex bedrock fracture patterns: A multipronged approach to resolve their evolution in space and time. *Tectonics*, *37*, 1030–1062. https://doi.org/10.1002/2017TC004763

Schultz, R. A., Okubo, C. H., & Wilkins, S. J. (2006). Displacement-length scaling relations for faults on the terrestrial planets. *Journal of Structural Geology*, *28*(12), 2182–2193. https://doi.org/10.1016/j.jsg.2006.03.034

Schumacher, E. (1975). Herstellung von >99,9997% ^{38}Argon für die ^{40}K-^{40}Ar Geochronologie. *Chimia*, *29*, 441–442.

Scotese, C. R., Gahagan, L. M., & Larson, R. L. (1988). Plate tectonic reconstructions of the Cretaceous and Cenozoic ocean basins. *Tectonophysics*, *155*(1-4), 27–48. https://doi.org/10.1016/0040-1951(88)90259-4

Sebai, A., Féraud, G., Bertrand, H., & Hanes, J. (1991). $^{40}Ar/^{39}Ar$ dating and geochemistry of tholeiitic magmatism related to the early opening of the Central Atlantic rift. *Earth and Planetary Science Letters*, *104*(2-4), 455–472. https://doi.org/10.1016/0012-821X(91)90222-4

Seton, M., Müller, R. D., Zahirovic, S., Gaina, C., Torsvik, T., Shephard, G., et al. (2012). Global continental and ocean basin reconstructions since 200 Ma. *Earth-Science Reviews*, *113*(3-4), 212–270. https://doi.org/10.1016/j.earscirev.2012.03.002

Solé, J., Delaloye, M., & Enrique, P. (1998). K–Ar ages in biotites and K–feldspars from the Catalan Coastal Batholith: evidence of a post-Hercynian overprinting. *Eclogae Geologicae Helvetiae*, *91*, 139–148.

Solum, J. G., van der Pluijm, B. A., & Peacor, D. R. (2005). Neocrystallization, fabrics and age of clay minerals from an exposure of the Moab Fault, Utah. *Journal of Structural Geology*, *27*(9), 1563–1576. https://doi.org/10.1016/j.jsg.2005.05.002

Sopeña, A., Virgili, C., Arche, A., Ramos, A., & Hernando, S. (1983). El Triásico. *Geologia de España*, *2*, 47–63.

Soria de Miguel, A. R. (1997). La sedimentación en las cuencas marginales del Surco Ibérico durante el Cretácico Inferior y su control estructural (Doctoral dissertation, Universidad de Zaragoza).

Soto, R., Casas-Sainz, A. M., Villalaín, J. J., Gil-Imaz, A., Fernández-González, G., Del Río, P., et al. (2008). Characterizing the Mesozoic extension direction in the northern Iberian plate margin by anisotropy of magnetic susceptibility (AMS). *Journal of the Geological Society*, *165*(6), 1007–1018. https://doi.org/10.1144/0016-76492007-163

Soto, R., Villalaín, J. J., & Casas-Sainz, A. M. (2008). Remagnetizations as a tool to analyze the tectonic history of inverted sedimentary basins: A case study from the Basque-Cantabrian basin (north Spain). *Tectonics*, *27*, TC1017. https://doi.org/10.1029/2007TC002208

Srivastava, S. P., Sibuet, J. C., Cande, S., Roest, W. R., & Reid, I. D. (2000). Magnetic evidence for slow seafloor spreading during the formation of the Newfoundland and Iberian margins. *Earth and Planetary Science Letters*, *182*(1), 61–76. https://doi.org/10.1016/S0012-821X(00)00231-4

Steiger, R. H., & Jäger, E. (1977). Subcommission on geochronology: Convention on the use of decay constants in geochronology and cosmochronology. *Earth and Planetary Science Letters*, *36*(3), 359–362. https://doi.org/10.1016/0012-821X(77)90060-7

Tapponnier, P., & Molnar, P. (1976). Slip-line field theory and large-scale continental tectonics. *Nature*, *264*(5584), 319–324. https://doi.org/10.1038/264319a0

Tapponnier, P., Peltzer, G., & Armijo, R. (1986). On the mechanics of the collision between India and Asia. *Geological Society, London, Special Publications*, *19*(1), 113–157. https://doi.org/10.1144/GSL.SP.1986.019.01.07

Torgersen, E., Viola, G., Zwingmann, H., & Harris, C. J. (2014). Structural and temporal evolution of a reactivated brittle-ductile fault: Part II. Timing of fault initiation and reactivation by K-Ar dating of synkinematic illite. *Earth and Planetary Science Letters*, *407*, 221–233. https://doi.org/10.1016/j.epsl.2014.09.031

Torgersen, E., Viola, G., Zwingmann, H., & Henderson, I. C. (2015). Inclined K-Ar illite age spectra in brittle fault gouges: Effects of fault reactivation and wall-rock contamination. *Terra Nova*, *27*(2), 106–113. https://doi.org/10.1111/ter.12136

Torres-López, S., Villalaín, J. J., Casas, A. M., Ouardi, H. E., Moussaid, B., & Ruiz-Martínez, V. C. (2014). Widespread Cretaceous secondary magnetization in the High Atlas (Morocco). A common origin for the Cretaceous remagnetizations in the western Tethys? *Journal of the Geological Society*, *171*(5), 673–687. https://doi.org/10.1144/jgs2013-107

Tugend, J., Manatschal, G., & Kusznir, N. J. (2015). Spatial and temporal evolution of hyperextended rift systems: Implication for the nature, kinematics, and timing of the Iberian-European plate boundary. *Geology*, *43*(1), 15–18. https://doi.org/10.1130/G36072.1

Vegas, R. (1992). The Valencia trough and the origin of the western Mediterranean basins. *Tectonophysics*, *203*(1-4), 249–261. https://doi.org/10.1016/0040-1951(92)90226-V

Villalaín, J. J., Fernández-González, G., Casas, A. M., & Gil-Imaz, A. (2003). Evidence of a Cretaceous remagnetization in the Cameros Basin (North Spain): Implications for basin geometry. *Tectonophysics*, *377*(1-2), 101–117. https://doi.org/10.1016/j.tecto.2003.08.024

Viola, G., Scheiber, T., Fredin, O., Zwingmann, H., Margreth, A., & Knies, J. (2016). Deconvoluting complex structural histories archived in brittle fault zones. *Nature Communications*, *7*(1), 13448. https://doi.org/10.1038/ncomms13448

Viola, G., Torgersen, E., Mazzarini, F., Musumeci, G., van der Lelij, R., Schönenberger, J., & Garofalo, P. S. (2018). New constraints on the evolution of the inner Northern Apennines by K-Ar dating of Late Miocene-Early Pliocene compression on the Island of Elba, Italy. *Tectonics*, *37*, 3229–3243. https://doi.org/10.1029/2018TC005182

Viola, G., Zwingmann, H., Mattila, J., & Käpyaho, A. (2013). K/Ar illite age constraints on the Proterozoic formation and reactivation history of a brittle fault in Fennoscandia. *Terra Nova*, *25*(3), 236–244. https://doi.org/10.1111/ter.12031

York, D., Evensen, N. M., López Martınez, M., & De Basabe Delgado, J. (2004). Unified equations for the slope, intercept, and standard errors of the best straight line. *American Journal of Physics*, *72*(3), 367–375. https://doi.org/10.1119/1.1632486

Ziegler, P. A. (1982). Faulting and graben formation in western and central Europe. *Philosophical Transactions of the Royal Society of London. Series A, Mathematical and Physical Sciences*, *305*(1489), 113–143. https://doi.org/10.1098/rsta.1982.0029

Ziegler, P. A., Cloetingh, S., Guiraud, R., & Stampfli, G. M. (2001). Peri-Tethyan platforms: Constraints on dynamics of rifting and basin inversion. In P. A. Ziegler, W. Cavazza, A. H. F. Robertson, & S. Crasquin-Soleau (Eds.), *Peri-Tethys Memoir 6*: Peri-Tethyan Rift/Wrench Basins and Passive Margins (Vol. 186, pp. 9–49). Paris: Mémoires du Muséum national d' Histoire naturelle.